Three-dimensional simulation of calcium waves and contraction in cardiomyocytes using the finite element method

Jun-ichi Okada,[1,2] Seiryo Sugiura,[2] Satoshi Nishimura,[3] and Toshiaki Hisada[2]

[1]Core Research for Evolutional Science and Technology of the Japan Science and Technology Agency, Saitama; [2]Computational Biomechanics Division, Institute of Environmental Studies, Graduate School of Frontier Sciences, The University of Tokyo, Tokyo; and [3]Department of Cardiovascular Medicine, Graduate School of Medicine, The University of Tokyo, Tokyo, Japan

Okada, Jun-ichi, Seiryo Sugiura, Satoshi Nishimura, and Toshiaki Hisada. Three-dimensional simulation of calcium waves and contraction in cardiomyocytes using the finite element method. Am J Physiol Cell Physiol 288: C510–C522, 2005. First published October 20, 2004; doi:10.1152/ajpcell.00261.2004.—To investigate the characteristics and underlying mechanisms of Ca^{2+} wave propagation, we developed a three-dimensional (3-D) simulator of cardiac myocytes, in which the sarcolemma, myofibril, and Z-line structure with Ca^{2+} release sites were modeled as separate structures using the finite element method. Similarly to previous studies, we assumed that Ca^{2+} diffusion from one release site to another and Ca^{2+}-induced Ca^{2+} release were the basic mechanisms, but use of the finite element method enabled us to simulate not only the wave propagation in 3-D space but also the active shortening of the myocytes. Therefore, in addition to the dependence of the Ca^{2+} wave propagation velocity on the sarcoplasmic reticulum Ca^{2+} content and affinity of troponin C for Ca^{2+}, we were able to evaluate the influence of active shortening on the propagation velocity. Furthermore, if the initial Ca^{2+} release took place in the proximity of the nucleus, spiral Ca^{2+} waves evolved and spread in a complex manner, suggesting that this phenomenon has the potential for arrhythmogenicity. The present 3-D simulator, with its ability to study the interaction between Ca^{2+} waves and contraction, will serve as a useful tool for studying the mechanism of this complex phenomenon.

cardiac muscle cell; excitation-contraction coupling; mechanoelectrical feedback; spiral wave; arrhythmia

CARDIAC MUSCLE CONTRACTION is regulated by rhythmic changes in intracellular Ca^{2+} concentration ($[Ca^{2+}]_i$). Under normal conditions, transsarcolemmal Ca^{2+} influx activated by membrane depolarization triggers synchronous Ca^{2+} release from the sarcoplasmic reticulum (SR) to bring about a uniform rise in $[Ca^{2+}]_i$ (Ca^{2+}-induced Ca^{2+} release, or CICR) (3). SR Ca^{2+} release can occur spontaneously without membrane depolarization to cause a local elevation of $[Ca^{2+}]_i$ that propagates throughout the cell in a wavelike pattern under certain conditions (8, 9, 30). Besides their importance in basic physiology, Ca^{2+} waves also have clinical relevance because a focal increase in $[Ca^{2+}]_i$ could activate a transient inward current and membrane depolarization, thus constituting a potentially arrhythmogenic event (2, 6). Accordingly, several studies have attempted to clarify the characteristics and underlying mechanisms of Ca^{2+} waves using single-cell (8, 15), multicellular (24), and whole heart (17) preparations.

Simulation studies have also been performed to integrate the experimental findings and provide a mechanistic explanation for them (1, 10, 16, 19, 29, 31). Basically, all of these models assumed that Ca^{2+} diffusion from one release site to another and CICR were the basic mechanisms, although various modifications were made by incorporating novel experimental findings, such as stochastic opening of ryanodine receptors (RyR) (16, 19) and anisotropy in diffusion (31). In addition, to reproduce the evolution of the characteristic wave pattern, including the spiral wave, simulations have been extended to two-dimensional (2-D) space (10, 16, 31). However, there are virtually no 3-D models that can be used for detailed analyses. Indeed, a recent study using a novel confocal microscope clearly demonstrated the 3-D nature of Ca^{2+} wave propagation (15), thus necessitating the development of a competitive 3-D model.

Another important step in excitation-contraction coupling that is not taken into consideration by current simulation models is myocyte contraction. Initially identified as a focal contraction (7), a Ca^{2+} wave definitely changes the distance between adjacent Ca^{2+} release sites as it propagates longitudinally along a myocyte. Furthermore, force development may change the affinity of troponin C (TnC) for Ca^{2+}, a major buffering system in the cytoplasm (13). Both of these aspects could potentially modulate Ca^{2+} wave propagation but have not yet been investigated fully.

In the present study, we have developed a 3-D simulator of Ca^{2+} wave propagation and contraction in cardiac myocytes in which the sarcolemma, myofibril, and Z line with Ca^{2+} release sites were modeled as separate structures using the finite element method. The wave front in 3-D space can be visualized in an arbitrary 2-D plane, facilitating detailed comparisons with the results obtained in earlier experimental and model studies. Furthermore, the effect of contraction on Ca^{2+} waves can be evaluated by simulation for the first time.

MATERIALS AND METHODS

CICR and Ca^{2+} diffusion model. The basic principle of the present simulation model was similar to those of previous reports (1, 10, 31) and is illustrated schematically in Fig. 1. In each sarcomere, Ca^{2+} release channels are located at the Z lines. Ca^{2+} released from the junctional SR (JSR) through a release channel (I_{rel}) is buffered by calmodulin (CaM) in the cytosol and TnC on the thin filament or sequestered by the nonjunctional SR (NSR) (I_{up}) and translocated to the JSR to replenish it (I_{tr}). The Ca^{2+} leak current (I_{leak}) was also
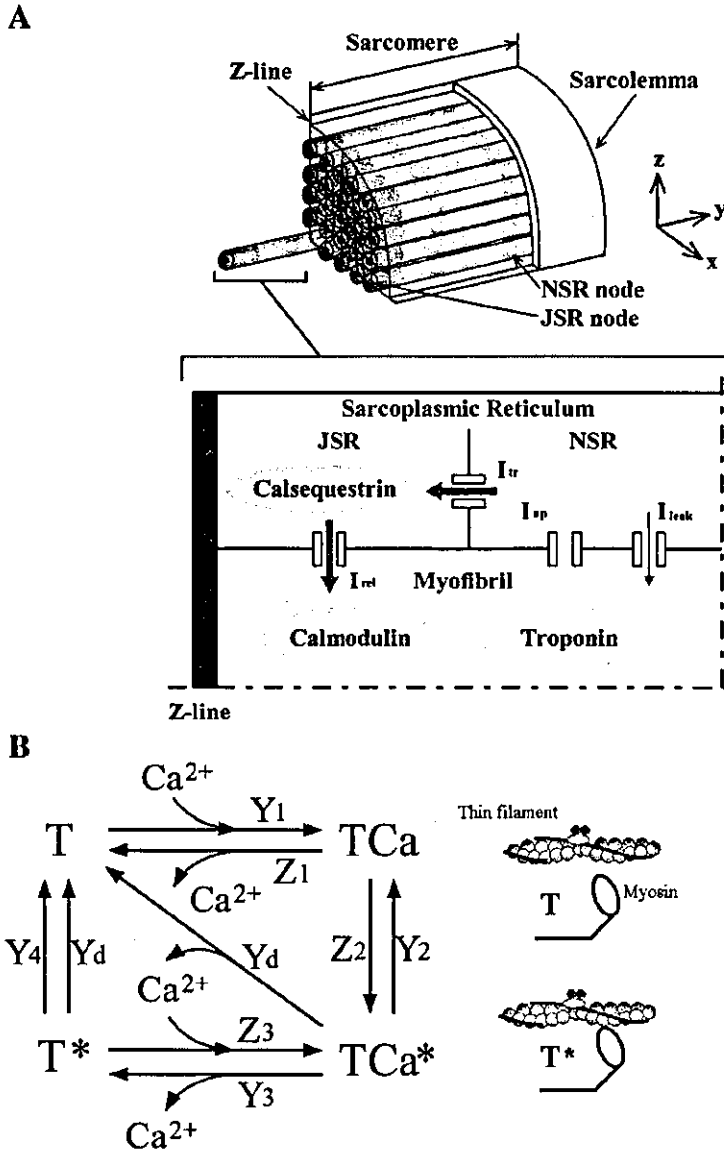
A

Z-line

Fig. 1. Simulation model. *A*: conceptual framework of the model. The cylindrical myocyte is occupied by myofibrils, and Ca²⁺ release sites [junctional sarcoplasmic reticulum (JSR) nodes] are located at the Z line (*top*). In each sarcomere, Ca²⁺ is released from the JSR at the Z line (I_{rel}) and diffuses into the cytoplasm, where it becomes bound by a buffering system [troponin C (TnC) and calmodulin (CaM)]. Free (unbound) Ca²⁺ is sequestered by the nonjunctional sarcoplasmic reticulum (NSR) (I_{up}) and translocates into the JSR (I_{tr}). I_{leak}: Ca²⁺ leakage from the NSR. *B, left*: 4-state model of the regulatory and contractile protein unit (T). Y_i (i = 1, 2, 3, 4, or d) and X_i (i = 1, 2, 3, 4, or d) are rate constants governing the transition between the states; *right*: physical entities of the states. TCa* and T* are force-bearing states.

B

modeled. The remaining free Ca²⁺ diffuses into the sarcomere space, and if the [Ca²⁺]ᵢ at the adjacent Z line exceeds a certain threshold, regenerative Ca²⁺ release takes place. In this analysis, we adopted a deterministic rule for triggering Ca²⁺ release (22), instead of a stochastic model (16, 19), for the following reasons: *1*) although a stochastic model may be a prerequisite for analyzing the evolution of Ca²⁺ from a Ca²⁺ spark, the present analysis exclusively studied the wave propagation; and *2*) implementation of a stochastic process heavily increases the computational burden. We admit that this model is not necessarily the best, but it should represent a reasonable starting point. For the same reasons, transsarcolemmal ion exchange processes were eliminated.

The mathematical formulation for [Ca²⁺]ᵢ dynamics is represented by the reaction-diffusion equation described below for the *y*-axis coordinate in the longitudinal direction and the *x*- and *z*-axis coordinates for the transverse directions (Fig. 1):

$$\frac{d[\text{Ca}^{2+}]_i}{dt} = \nabla \cdot (D_c \nabla [\text{Ca}^{2+}]_i) + f([\text{Ca}^{2+}]_i) \qquad (1)$$

where *dt* is development over time, D_c is a diagonal matrix describing the diffusivity of Ca²⁺, and $f([\text{Ca}^{2+}]_i)$ describes the kinetics of Ca²⁺ transport into and out of the cytoplasm. In this analysis, the diffusion coefficient for Ca²⁺ (diagonal elements of D_c) was set to 1.0 μm²/ms for the longitudinal (*y*-axis) direction and 0.5 μm²/ms for the transverse (*x*- and *z*-axis) directions on the basis of previous experimental studies (16, 27). Modifications were made depending on the location to yield the following equations.

At the nodes where NSR is facing cytoplasm (NSR node in Fig. 1*A*, *top*):

$$\frac{d[\text{Ca}^{2+}]_i}{dt} = \nabla \cdot (D_c \nabla [\text{Ca}^{2+}]_i) + (I_{leak} - I_{up}) \frac{V_{\text{NSRnode}}}{V_{\text{myonode}}}$$

$$- \frac{d([\text{CaM} - \text{Ca}^{2+}])}{dt} - \frac{d([\text{TnC} - \text{Ca}^{2+}])}{dt} \qquad (2)$$

Table 1. *Mechanical properties of myocytes*

Parameter	Shell Element, Sarcolemma	Truss Element		Solid Element		
		Myofibril	Z line	Intercalated disk	Cytoplasm	Nucleus
Young's modulus, kPa	10	Negroni's model (Ref. 25)	500	500	0.01	10
Poisson ratio	0.45			0.45	0.45	0.45
Thickness, μm	1					
Diameter, μm		1	0.01			

At the nodes where JSR is facing cytoplasm (JSR node in Fig. 1*A*, *top*):

$$\frac{d[Ca^{2+}]_i}{dt} = \nabla \cdot (D_c \nabla [Ca^{2+}]_i) + I_{relClCR} \frac{V_{JSRnode}}{V_{myonode}}$$
$$- \frac{d([CaM - Ca^{2+}])}{dt} - \frac{d([TnC - Ca^{2+}])}{dt} \qquad (3)$$

where (TnC − Ca²⁺) is the Ca²⁺ buffered by TnC and (CaM − Ca²⁺) is the Ca²⁺ buffered by CaM. At nodes corresponding to the nucleus, permeability to Ca²⁺ diffusion was altered to examine its effect. We assumed that the nuclear membrane does not act as a diffusion barrier (4).

Muscle contraction model. To relate the local [Ca²⁺]ᵢ to cross-bridge kinetics and force generation, we adopted the theoretical formalism proposed by Negroni and Lascano (25). Briefly, the TnC state (regardless of whether bound to Ca²⁺) and the cross-bridge state (attached or detached) are combined into four states as shown in Fig. 1*B*: *1*) TnC is bound to Ca²⁺, and the cross bridge is attached (TnC*); *2*) TnC is not bound to Ca²⁺, but the cross bridge remains attached (T*); *3*) TnC is bound to Ca²⁺, but the cross bridge is detached (TCa); and *4*) TnC is not bound to Ca²⁺, and the cross bridge is detached (T). The transitions between these four states are governed by the evolutional equations described in the APPENDIX. In the analysis examining the effect of the affinity of TnC for Ca²⁺, we changed the rate constant for Ca²⁺ binding to TnC (Y_1). Of the four states, TCa* and T* contribute to force generation such that the active force per unit length (F_b) is as follows:

$$F_b = A \cdot ([TCa^*] + [T^*]) \cdot h \qquad (4)$$

where A is a constant and h is the cross-bridge elongation. The sarcomere shortening concomitant with the detachment of a certain proportion of cross bridges further decreases the number of attached cross bridges through two additional paths whereby TCa* and T* decrease depending on the velocity of the shortening. This mechanism is known as shortening-induced deactivation (13).

The passive property is characterized by the force developed by the parallel elastic component (F_p):

$$F_p = K \cdot (L - L_0)^5 \qquad (5)$$

where K is a constant, L is the length of a half-sarcomere (L), and L_0 is the unstressed length of L.

The total muscle force (F) can be expressed as the sum of the active and passive forces as follows:

$$F = F_b + F_p \qquad (6)$$

Cell geometry and finite element modeling. We assumed the geometry of the cell to be a cylinder with a diameter of 16 μm and a height of 104 μm. The Z lines, each of which is represented by a truss element network, are spaced at 2-μm intervals. The myofibrils were modeled by 113 vertical truss elements within a sarcomere, each of which had a diameter of 1 μm. They occupied 47% of the cross section. These values were estimated from Figs. 1 and 2 in Lipp and Niggli (21) and Fig. 2 in Ishida et al. (15). The sarcolemma including the cytoskeleton was represented by mixed interpolation of tensorial

component shell elements (11), and the cytoplasm was represented by hexahedral bilinear solid elements. The nucleus had a diameter of 5 μm and a height of 10 μm (15). Its center was located 15 μm from the end in the longitudinal direction and 4 μm from the center in the cross section. We also estimated these values from data in the literature (15, 21). There were 15,168 solid elements, 16,884 truss elements, and 5,248 shell elements, and the total number of degrees of freedom was 64,401. As a constitutive law for these finite elements, we assumed an isotropic St. Venant's hyperelastic model, in which the strain energy function is calculated as follows (5):

$$W = \frac{1}{2}\left(\frac{Ev}{(1+v)(1-2v)}\right)(trE)^2 + \left(\frac{E}{2(1+v)}\right)E:E \qquad (7)$$

where E is the Green-Lagrange strain tensor, E is the Young's modulus, and v is the Poisson's ratio. The colon denotes the scalar products of two second-order tensors (23). Differentiation of the above equation with respect to E gives the second Piola-Kirchhoff stress tensor as follows:

$$S = \left[\left(\frac{Ev}{(1+v)(1-2v)}\right)I \otimes I + 2\left(\frac{E}{2(1+v)}\right)I\right]:E = C:E \qquad (8)$$

where I is the second-order unit tensor, and ($I \otimes I$) and I are the fourth-order tensors that operate on E as ($I \otimes I$) : $E = (trE)I$ and I : $E = E$, respectively. C is the fourth-order elasticity tensor that results in a constant due to the quadratic form of W, and S is the second Piola-Kirchhoff stress. These equations were defined using the coordinate system shown in Fig. 1. Because of the lack of numeric data on the material properties of the subcellular components, these values were adjusted to reproduce the cardiac muscle properties determined at the tissue level (20). The model-adjusted material properties used in this simulation are summarized in Tables 1–4.

Ca²⁺ diffusion was analyzed by a Galerkin method-based finite element method in which bilinear hexahedral solid elements are used with the same mesh used for the cytoplasm. It has been shown that a cluster of SR Ca²⁺ channels is involved in the formation of a Ca²⁺ spark (i.e., Ca²⁺ release unit, or CRU) (21, 27). It also has been shown that these CRUs are discretely located at Z lines (27). CRUs were

Table 2. *Cell geometry*

Parameter	Definition	Value
L	Cell length	104 μm
r	Cell radius	8 μm
V_{cell}	Cell volume	20.9 × 10⁻⁶ μl
V_{myo}	Cytoplasm volume	V_{cell} × 0.47 = 9.83 × 10⁻⁶ μl
V_{mito}	Mitochondria volume	V_{cell} × 0.36 = 7.53 × 10⁻⁶ μl
V_{SR}	SR volume	V_{cell} × 0.035 = 0.732 × 10⁻⁶ μl
V_{NSR}	NSR volume	V_{cell} × 0.0315 = 0.659 × 10⁻⁶ μl
V_{JSR}	JSR volume	V_{cell} × 0.0035 = 0.0732 × 10⁻⁶ μl
V_{other}	Other volume	V_{cell} × 0.115 = 2.405 × 10⁻⁶ μl

SR, sarcoplasmic reticulum; JSR, junctional SR; NSR, nonjunctional SR; $V_{NSRnode}$, V_{NSR}/(FE node numbers corresponding to NSR = 11,744) (μl); $V_{JSRnode}$, V_{JSR}/(FE node numbers corresponding to JSR = 5,986) (μl); $V_{myonode}$, V_{myo}/(FE node numbers corresponding to cytoplasm = 17,730) (μl).

Table 3. *Initial conditions of stimulation*

Parameter	Normal Contraction and Ca²⁺ Wave Collision	Cell Contraction with 3-D Ca²⁺ Wave Propagation
$[Ca^{2+}]_i$	0.00014 mmol/l	0.000115 mmol/l
$[Ca^{2+}]_{NSR}$	1.889 mmol/l	1.661 mmol/l
$[Ca^{2+}]_{JSR}$	1.842 mmol/l	1.628 mmol/l
$[CSQN - Ca^{2+}]$	6.972 mmol/l	6.705 mmol/l
$[CaM - Ca^{2+}]$	0.002769 mmol/l	0.002304 mmol/l
[TCa]	0.2006×10^{-2} mmol/l	0.1678×10^{-2} mmol/l
[TCa*]	0.8131×10^{-4} mmol/l	0.6029×10^{-4} mmol/l
[T*]	0.4638×10^{-4} mmol/l	0.3884×10^{-4} mmol/l
[T]	0.4866×10^{-2} mmol/l	0.5223×10^{-2} mmol/l

3-D, three-dimensional. See text for additional definitions.

modeled at the nodes on the cross-sectioned planes corresponding to the Z lines (Fig. 1A, *top*). Ca^{2+} was sequestered or released on the basis of *Eq. 2* and *3*, and the diffusion was simulated using the finite element method, in which a time step of $\Delta t = 0.01$ ms was used. The Ca^{2+} concentration thus computed was applied to Negroni and Lascano's model (25) to evaluate the contraction force. Next, the total muscle force was calculated using *Eqs. 4–6* such that the new internal force of the truss element was determined for the finite element deformation analysis of the cell model. The resultant deformation of the myofibril was returned to the finite element model of the Ca^{2+} diffusion analysis and Negroni and Lascano's model. Excitation-contraction coupling was thus realized. Excitation-contraction coupling analyses were performed for every 200 steps of the Ca^{2+} diffusion analysis.

Experiments. Although originally recognized as spontaneous myofilament oscillation within cells (7), sarcomere dynamics during Ca^{2+} waves are not well understood. We monitored the sarcomere length in isolated rat cardiomyocytes during Ca^{2+} waves. Hearts were removed

from adult male Wistar rats (200–300 g) that were under pentobarbital sodium anesthesia (50 mg/kg), and the left ventricular myocytes were isolated using enzymatic dissociation as described previously (35). Myocytes were suspended in 1.8 mmol/l Ca^{2+} HEPES-Tyrode solution (in mmol/l: 137 NaCl, 5.4 KCl, 1.8 CaCl₂, 0.5 MgCl₂, 0.33 NaH₂PO₄, 5 HEPES, and 5 glucose, adjusted to pH 7.4 with NaOH at 22°C), transferred to a silicone-coated (Sigmacote; Sigma) glass chamber, and viewed using an inverted microscope (×40 objective, IX71; Olympus). During spontaneous Ca^{2+} waves, we recorded the sarcomere length in the middle region of the sarcomere using online Fourier analysis of digitized myocyte images (SarcLen; IonOptix). From simultaneously recorded myocyte images, we measured the cell length using NIH Image software (National Institutes of Health, Bethesda, MD). To visualize Ca^{2+} waves, myocytes were loaded with fluo-3 by incubation in the 1.8 mmol/l Ca^{2+} HEPES-Tyrode solution containing 5 mol/l fluo-3 AM (Molecular Probes, Eugene, OR) for 45 min at room temperature. Myocytes were observed using a confocal microscope (CSU22; Yokogawa) equipped with a charge-coupled device camera (EVM285SPD; Texas Instruments).

RESULTS

Simulation of normal excitation and Ca^{2+} waves. Simulated cell shortening and color-coded $[Ca^{2+}]_i$ during normal excitation are shown as time-lapse images in Fig. 2. In this case, normal excitation was simulated by homogeneously raising the $[Ca^{2+}]_i$ above the threshold (0.2 μmol/l; Refs. 18, 19) at *time 0*. Ca^{2+} release was evoked uniformly and instantaneously (0.1 s) along the whole cell length, such that the cell contracted quickly (0.1–0.3 s). When a localized Ca^{2+} spark occurred (simulated as Ca^{2+} release from a single release site; 0.05 s), it evolved into a Ca^{2+} wave and spread in opposite directions at equal velocity (Fig. 3). However, in this case, the Ca^{2+} wave

Table 4. *Model parameters*

| Parameter	Definition	Value
$K_{m,up}$	Half-saturation concentration of I_{up}	0.00092 mmol/l
I_{up}	Maximum current through the I_{up} channel	0.00875 mmol/l/ms
$K_{m,nucleus}$	Half-saturation concentration of $I_{nucleus}$	0.00092 mmol/l
$I_{nucleus}$	Maximum current through the $I_{nucleus}$ channel	0.0015 mmol/l/ms
$[Ca^{2+}]_{NSR}$	Maximum Ca^{2+} buffered in the NSR	15 mmol/l
τ_t	Time constant of Ca^{2+} transfer from the NSR to the JSR	180 ms
$G_{relCICR}$	Rate constant of Ca^{2+} release from the JSR to the cytoplasm due to CICR	21/ms ·
τ_{on}	Time constant	10 ms
τ_{off}	Time constant	10 ms
[CSQN]	Maximum Ca^{2+} buffered by CSQN	10 mmol/l
$K_{m,CSQN}$	Equilibrium constant for buffering by CSQN	0.8 mmol/l
Y_1	Rate parameter of Ca^{2+} binding to TnC	78 l/mmol·ms
Y_2	Rate parameter of cross-bridge attachment to a thin filament site associated with TCa	0.104 l/ms
Y_3	Rate parameter of Ca^{2+} release from TCa*	0.36 l/ms
Y_4	Rate parameter of T* detachment	0.2 l/ms
Diag (D_c)	Diagonal matrices describing the diffusivity	(0.5, 1.0, 0.5) μm²/ms
Z_1	Rate parameter of Ca^{2+} unbinding from TCa	0.36 l/ms
Z_2	Rate parameter of TCa* detachment	0.0013 l/ms
Z_3	Rate parameter of Ca^{2+} rebinding to T*	3,120 l/mmol·ms
Y_d	Parameter determining the influence of dX/dt on Q_{d1} and Q_{d2}	9,000 ms/μm²
[T]	Total TnC	0.07 mmol/l
R	Exponential parameter characterizing the L dependence of $[TCa]_{eff}$	20 l/μm²
L_a	Optimal L for maximum $[TCa]_{eff}$	1.17 μm
[CaM]	Maximum Ca^{2+} buffered by CaM	0.05 mmol/l
$K_{m,CaM}$	Equilibrium constant for buffering by CaM	0.00238 mmol/l
K	Proportional parameter of the parallel elastic component of F_p	10,000 mN/mm²/μm⁵
l_0	Unstressed L characterizing F_p	0.97 μm
h_c	Cross-bridge elongation at steady-state L	0.005 μm
A	Stiffness of the equivalent cross-bridge elastic element referred to concentrations	1,800 mN·l/mm²/μm/μmol
B	Proportionality parameter for dX/dt	1.2 l/ms

A
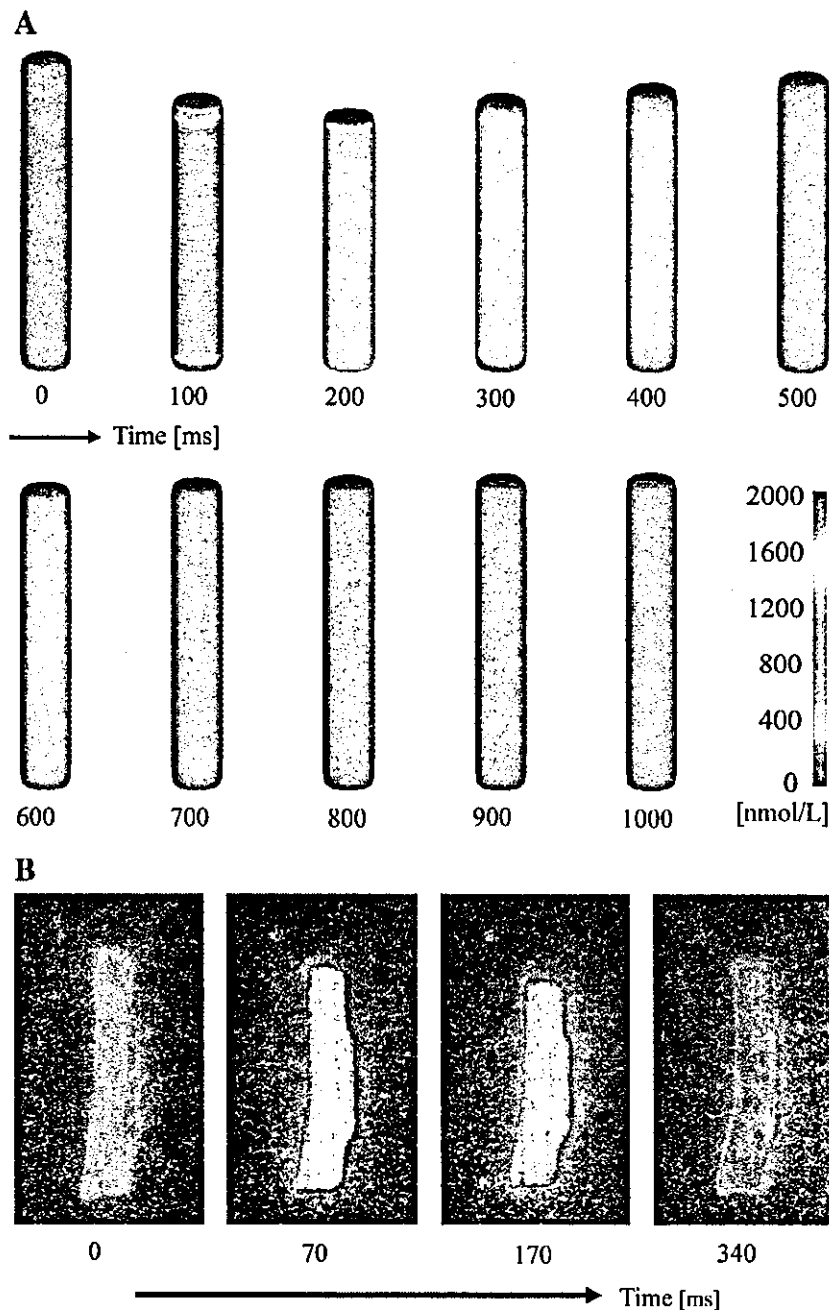
Fig. 2. *A*: time-lapse images of a three-dimensional (3-D) simulation showing intracellular Ca^{2+} concentration ($[Ca^{2+}]_i$) changes and myocyte contraction during normal excitation. *B*: Ca^{2+} signal (fluo-3) and contraction of a single rat ventricular myocyte. $[Ca^{2+}]_i$ rises and then decays rapidly throughout the cell.

B

could induce only weak contraction (0.1–0.3 s), consistent with our experimental observations (Figs. 2*B* and 3*B*) and those in another report (24). We also simulated a case in which two independent Ca^{2+} waves collided (Fig. 4). Waves were initiated at both ends of the cell and propagated toward the center. Because the propagation velocity was the same, the two waves collided in the middle (0.4 s) and then disappeared (0.6 s). This simulation also reproduced our experimental findings (Fig. 4*B*) and those described in a previous report (8).

Wave propagation velocity. In this study, the Ca^{2+} wave propagation velocity was 140 μm/s under the control conditions (resting $[Ca^{2+}]_i = 0.13$ μmol/l, $[Ca^{2+}]_{JSR} = 1.86$ mmol/l).

Because previous experimental studies (24) suggested a dependence of the propagation velocity on Ca^{2+} loading of the cell, we evaluated the effect of the SR Ca^{2+} content on the propagation velocity to investigate whether they had a linear relationship with each other (Fig. 5*A*). The dependence was confirmed when either the myocyte was allowed to shorten (solid line) or its length was fixed (broken line). We changed the Ca^{2+} content of the JSR because Miura et al. (24), in the relevant experiment, estimated SR Ca^{2+} loading on the basis of the released Ca^{2+}, which presumably was stored in the JSR. We examined the effect of NSR Ca^{2+} store to find a similar result with JSR Ca^{2+} store (data not shown). We think this is

A

0   50   100   200   300   400   500

➝ Time [ms]

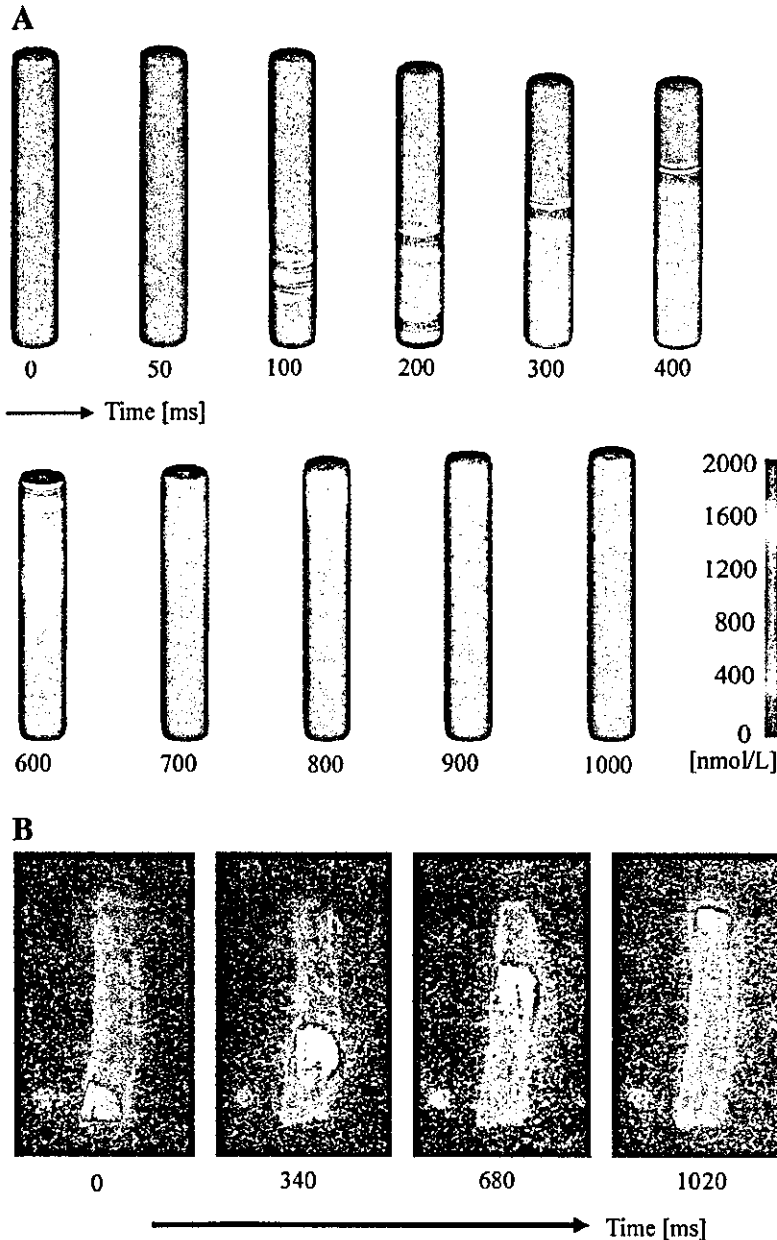600   700   800   900   1000   [nmol/L]

2000
1600
1200
800
400
0

Fig. 3. *A*: time-lapse images of a 3-D simulation during a Ca²⁺ wave. The cell shortening is moderate in length (shortening fraction 10%) but long lasting compared with normal excitation (Fig. 2; shortening fraction 20%). *B*: Ca²⁺ wave observed in the same myocyte shown in Fig. 2*B*. The cell shortening is moderate compared with Fig. 2*B*.

B

0   340   680   1020

➝ Time [ms]

because the Ca²⁺ content of NSR and JSR are closely related. The difference in velocity between the two conditions is discussed below. When we changed the affinity of TnC for Ca²⁺ by altering the rate constant for Ca²⁺ binding with TnC (Y_1 in Fig. 1*B*), the velocity decreased as the affinity increased (Fig. 5*B*). These results are consistent with previous experimental findings (8, 24) and therefore validate the basic assumption of the current simulation model.

Effect of contraction on Ca²⁺ waves. In all of the analyses described above, the myocyte was allowed to shorten in the unloaded condition. Under physiological conditions, however, each myocyte is connected to adjacent myocytes and thus under constraint. Accordingly, we simulated a case in which the myocyte length was held constant under load (isometric

condition). In Fig. 6, the propagations of both the Ca²⁺ (*left* column) and contraction (sarcomere strain pattern; *right* column) waves are color coded and shown for the unloaded (Fig. 6*A*) and isometric (Fig. 6*B*) conditions with time on the *x*-axis and longitudinal location on the *y*-axis. The Ca²⁺ waves propagated smoothly under both conditions, but the unloaded Ca²⁺ wave reached the end of the cell earlier because of cell shortening. On the other hand, the contraction (sarcomere shortening) wave exhibited different patterns of propagation depending on the mode of contraction. In contrast to the very smooth propagation in the unloaded condition (Fig. 6*A*, *right*), isometric contraction produced a heterogeneous progression of sarcomere length distribution (Fig. 6*B*, *right*). Such heterogeneity in the strain distribution cannot be explained by the
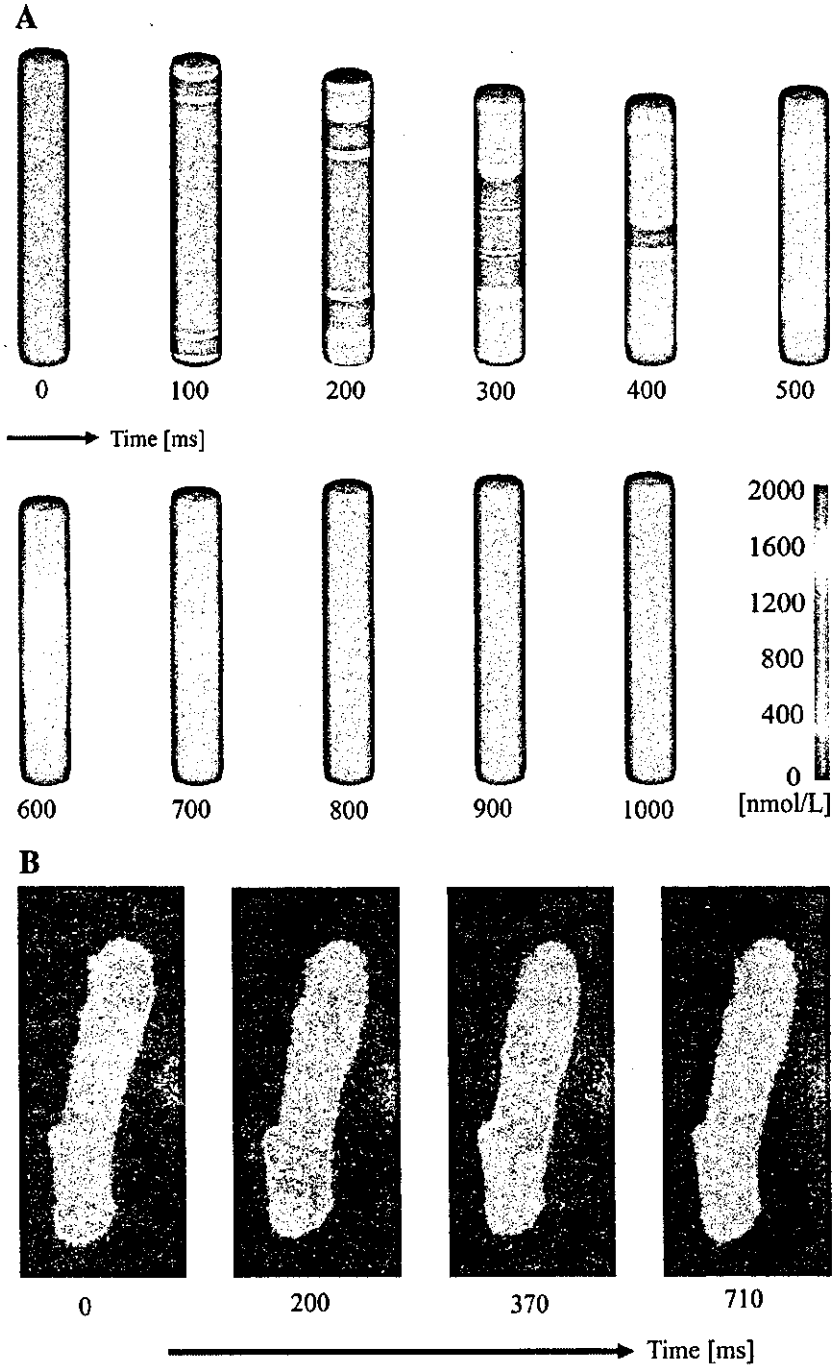
A

B

Fig. 4. *A*: time-lapse images of a 3-D simulation showing the collision and disappearance of 2 independent Ca²⁺ waves. *B*: collision of the Ca²⁺ waves observed in the experiment.

[Ca²⁺]ᵢ distribution or the stress equilibrium on the basis of the static stress-strain relationship. In Negroni and Lascano's contraction model (25), shortening deactivation is implemented by the force deficit terms Q_{d1} and Q_{d2}, formulated as follows (see also the APPENDIX):

$$Q_{d1} = Y_d \cdot \left(\frac{dX}{dt}\right)^2 \cdot [T^*] \qquad (9)$$

$$Q_{d2} = Y_d \cdot \left(\frac{dX}{dt}\right)^2 \cdot [TCa^*], \qquad (10)$$

where dX/dt is the strain rate. We hypothesized that the complex pattern of contraction was induced by the strain rate, depending on the heterogeneity of the stress-strain relationship. In other words, in the proximity of active shortening (blue region), the sarcomere becomes softer because of the high $(dX/dt)^2$ value and local stretching, thus leading to the complex strain pattern in Fig. 6*B*. To test this hypothesis, we repeated the simulation under the isometric condition without the force deficit terms Q_{d1} and Q_{d2} and compared the result with the original calculation (Fig. 6*C*). The results clearly revealed that
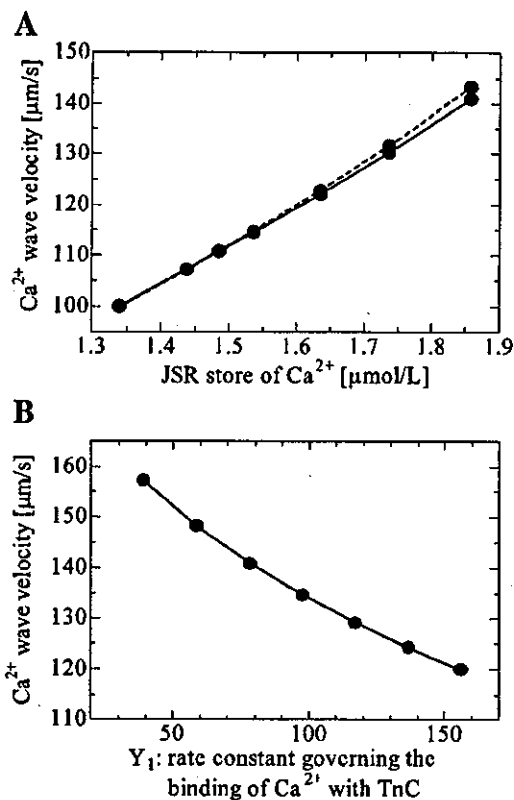
Fig. 5. *A*: relationships between the SR Ca²⁺ load and the Ca²⁺ wave propagation velocity under shortening (solid line) and isometric (broken line) conditions. *B*: relationship between the affinity of TnC for Ca²⁺ and the Ca²⁺ wave propagation velocity under shortening conditions.

the complex pattern disappeared, thus supporting our hypothesis. A similar tendency was observed experimentally in isolated cardiomyocytes. During a Ca²⁺ wave, each myocyte exhibited prolonged shortening to a small extent (<20 μm) (Fig. 7, *A* and *B*, broken lines). However, because the intensity of the cell attachment to the glass surface varied considerably, thereby applying different loads to the contracting cell, the shortening length of each myocyte differed significantly. In a myocyte that shortened by nearly 20 μm (Fig. 7*A*, broken line), the sarcomere shortened smoothly by ~0.2 μm (Fig. 7*A*, solid line). On the other hand, in a myocyte shortened to a lesser extent (<10 μm), the sarcomere stretched first before it shortened (Fig. 7*B*, solid line). In the simulation, heterogeneity in the sarcomere strain had an influence on the propagation velocity of the Ca²⁺ wave. Although the color-coded presentations appeared the same (Fig. 6, *left*), close examination of the isometric Ca²⁺ wave revealed local heterogeneity in the propagation velocity (Fig. 8*A*, broken line), in clear contrast to that of unloaded shortening (Fig. 8*A*, solid line). However, when averaged over its entire course, the propagation velocity of the Ca²⁺ wave was slightly faster in the isometric condition (Fig. 8*B*, thin solid line), while the velocity of the contraction wave was faster in the unloaded condition (Fig. 8*B*, thick broken line).

Evolution of spiral waves in 3-D space. We examined the effect of the nucleus on Ca²⁺ wave propagation by initiating Ca²⁺ sparks in the proximity of the nucleus. Each nucleus was

treated not only as a region lacking a releasable Ca²⁺ pool but also as a buffering pool (21). In the short-axis slice, the Ca²⁺ wave spread around the nucleus, creating a spiral wave (Fig. 9*A*, *top*). In the longitudinal plane (*middle* and *bottom*), however, the evolution of the wave differed significantly depending on the depth of the slice. As shown in Fig. 9 (*middle*), the spiral wave was observed only in the slice including the nucleus. This result is consistent with the experimental observations in Ishida et al. (15), thus substantiating the importance of 3-D simulation. The propagation velocity of a spiral wave was 76 μm/s and thus slower than a planar wave. When the buffering power of the nucleus was excluded, formation of a spiral wave was not evident (data not shown) and the propagation velocity became slightly faster (81 μm/s).

DISCUSSION

Assumption of rapid Ca²⁺ buffering. The role of buffering in Ca²⁺ waves has been studied in detail by Keizer and colleagues (28, 33). On the basis of a simulation model, they showed that assumption of rapid buffering is valid if the equilibration time of the buffer is much smaller than the time required for Ca²⁺ diffusion across a region of the size of a typical gradient. Quantitatively, their criteria are expressed as follows:

$$\tau = \frac{1}{(k^- + k^+([Ca^{2+}] + [B]))} \ll \frac{L^2}{D_c} \qquad (11)$$

where τ is the equilibration time constant for the buffer, k^- and k^+ are the rate constants for the binding and dissociation between Ca²⁺ and the buffer, respectively, [B] is the concentration of the buffer, L is the characteristic length of the [Ca²⁺]ᵢ profile, and D_c is the diffusion constant of Ca²⁺. Calculating τ for CaM with the values used in our study ([Ca²⁺]ᵢ = 1 μmol/l, [CaM − Ca] = 50 μmol/l) and those in the previous report by Smith et al. (28), the τ value for CaM is ~0.00004. This value is much smaller than the L^2/D_c value calculated in the present study (L^2/D_c: 0.001, $L = 1$ μm, and $D_c = 1,000$ μm²/s), thus indicating that the assumption of rapid buffering can be applied to the present simulation.

In this simulation, we treated CaM as stationary for the sake of simplicity. According to Smith et al. (28), however, the existence of a mobile buffer reduces the effective diffusion coefficient for Ca²⁺ (D_{eff}) as follows:

$$D_{eff} = \beta(D_c + \gamma_m D_m) \qquad (12)$$

where β is the differential fraction of free to bound Ca²⁺ (< 1), and

$$\gamma = \frac{K_m[B_m]_T}{(K_m + [Ca^{2+}]_i)^2} \qquad (13)$$

where K_m is the dissociation constant of the mobile buffer, $[B_m]_T$ is the total concentration of the mobile buffer, and D_m is the diffusion constant for the mobile buffer. Again, calculating $\gamma_m D_m$ for CaM, the result is ~330 μm²/s for the conditions used in this simulation ($K_m = 2.4$ μmol/l, $[B_m]_T = 50$ μmol/l, [Ca²⁺]ᵢ = 1 μmol/l, $D_m = 32$ μm²/s). This would amount to ~33% of the D_c used in this study, thus leading to an underestimation of the propagation velocity.
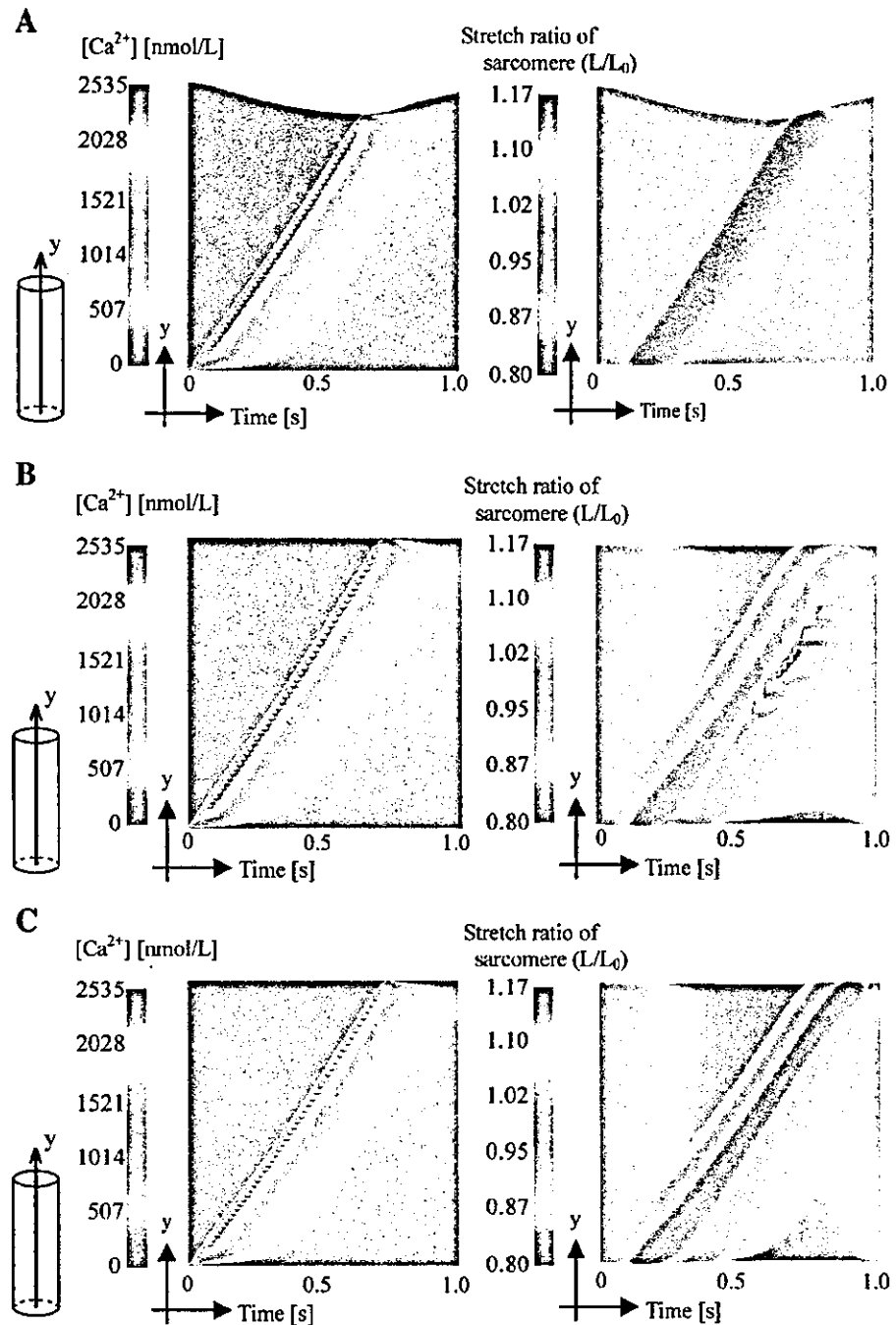
Fig. 6. *A*: color-coded presentation of the spatiotemporal distribution of [Ca^{2+}]$_i$ (*left*) and the change in sarcomere length (*L/L₀*) (*right*) during Ca^{2+} wave propagation in the unloaded condition. *B*: color-coded presentation of the spatiotemporal distribution of [Ca^{2+}]$_i$ (*left*) and the change in sarcomere length (*L/L₀*) (*right*) during Ca^{2+} wave propagation under the constraint of constant cell length. *C*: color-coded presentation of the spatiotemporal distribution of [Ca^{2+}]$_i$ (*left*) and the change in sarcomere length (*L/L₀*) (*right*) during Ca^{2+} wave propagation under the isometric condition without the force deficit terms Q_{d1} and Q_{d2}.

Comparisons with previous studies. Studies of Ca^{2+} waves have been promoted by a number of breakthroughs in experimental technique, such as the application of Ca^{2+} indicators (26, 32), laser confocal microscopy, and digital image processing (8, 15, 24, 34). Along with these developments, simulation studies also have made a significant contribution to the understanding of this complex phenomenon involving various intracellular dynamics (1, 10, 16, 19, 29). Most of these studies are based on a mechanistic model in which the diffusion of Ca^{2+} released by Ca^{2+} sparks induces a regenerative Ca^{2+} release from the adjacent SR (8). Our simulation model also adopted

this conceptual framework and used the mathematical formulation of SR Ca^{2+} uptake, relocation, release, and intracellular binding proposed by Luo and Rudy (22). Although transsarcolemmal ion flux was ignored, our model could successfully reproduce the bidirectional propagation and disappearance after collision of Ca^{2+} waves together with the changes in cell length (Figs. 2–4). Furthermore, dependence of the Ca^{2+} wave propagation velocity on intracellular Ca^{2+} loading and affinity binding was also confirmed (24).

On the other hand, we did not incorporate the stochastic nature of Ca^{2+} sparks (16, 19), owing to limitations in com-
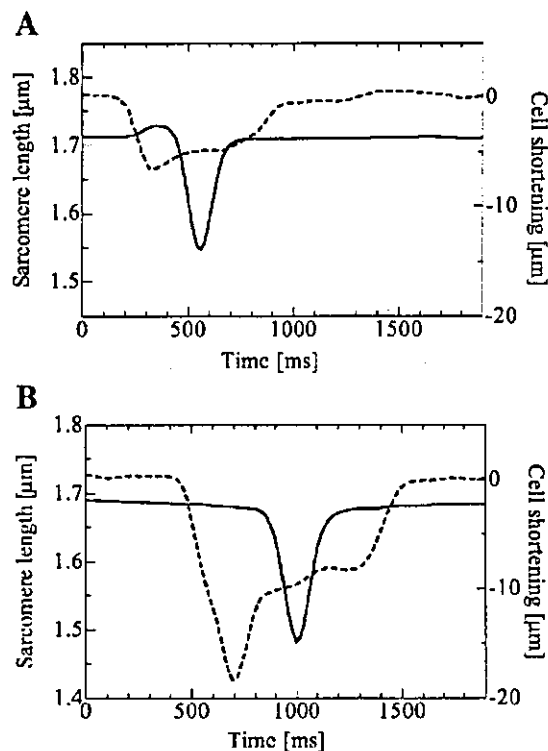
A

B

Fig. 7. Cell length (broken line) and sarcomere length (solid line) under low (A) and high (B) load during Ca²⁺ wave propagation observed experimentally in isolated rat cardiomyocytes.

clarify these apparently contradictory results, further studies are required in both the experimental and simulation fields.

Nucleus and Ca²⁺ waves. Although 3-D simulations of Ca²⁺ waves have been reported (16, 31), most have been simple extrapolations of 2-D simulations. Considering the axisymmetric and repetitive structure of cardiomyocytes, this type of simplification may be validated. However, a recent report by Ishida et al. (15) showing the evolution of spiral waves in 3-D space highlights the necessity for complete 3-D simulation, especially in the presence of the nucleus as an obstacle to propagation. The role of the nucleus in the generation of spiral waves was investigated by Dupont et al. (10), but their 2-D simulation could not provide an answer to the vertical heterogeneity in wave propagation reported by Ishida et al. (15). Although our simulation model successfully reproduced the previously reported generation, velocity, and vertical heterogeneity of spiral waves (15, 21), we could not model the oscillatory waves emanating from the spiral waves (21). Generation of repetitive waves may require a different model for CICR. Because recent studies have revealed spreading of Ca²⁺ waves over trabeculae (24) and the whole heart (17), oscillatory waves may be an origin of fatal arrhythmia. Further studies are required to clarify the conditions for generating oscillatory waves.

Study limitations. As stated repeatedly, we excluded the transsarcolemmal ion flux from the analysis because of limi-
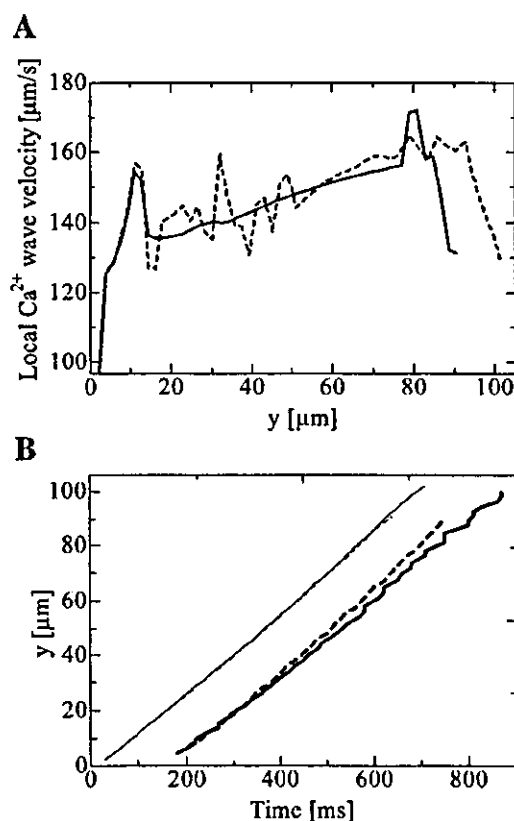
puter power. In this sense, our simulator is ineffective for studying the evolution process of Ca²⁺ waves from partial Ca²⁺ sparks but can be used to investigate the coupling of a Ca²⁺ wave with local sarcomere contraction and complete simulation in 3-D space, which were not achieved by previous simulators.

Effect of contraction on Ca²⁺ waves. Using the cardiac contraction model of Negroni and Lascano (25), we coupled $[Ca^{2+}]_i$ with contraction to evaluate its influence on Ca²⁺ waves. To our knowledge, this is the first attempt to couple these aspects of cardiomyocytes using full 3-D simulation. Currently, it requires ~37 h to complete the computation for a single contraction (2 s) using a CPU running at 3.2 GHz with 2-GB memory. Although the limitations in computational power forced us to adopt this relatively simple model, the analysis revealed interesting findings. As expected on the basis of experimental observations, there was significant internal shortening and stretching along the course of Ca²⁺ wave propagation while the cell length was kept constant (Fig. 6B, *right*). These changes in sarcomere length can influence a Ca²⁺ wave in at least two ways. First, strain applied to the thin filament increases the affinity of TnC for Ca²⁺ (14) and thus potentially slows the propagation. This property was incorporated into our model as a decrease in Ca²⁺ from TnC as the sarcomere shortened. Second, sarcomere shortening can decrease the diffusion distance to accelerate the propagation. Through these mechanisms, isometric contraction is expected to slow the propagation. In our analysis, however, isometric contraction exhibited a complex velocity pattern (Fig. 7A). To

A

B

Fig. 8. A: local variation in the Ca²⁺ wave propagation velocity under unloaded (solid line) and isometric (broken line) conditions. B: propagation of the contraction (thick lines) and Ca²⁺ (thin lines) waves under unloaded (broken lines) and constant cell length (solid lines) conditions.
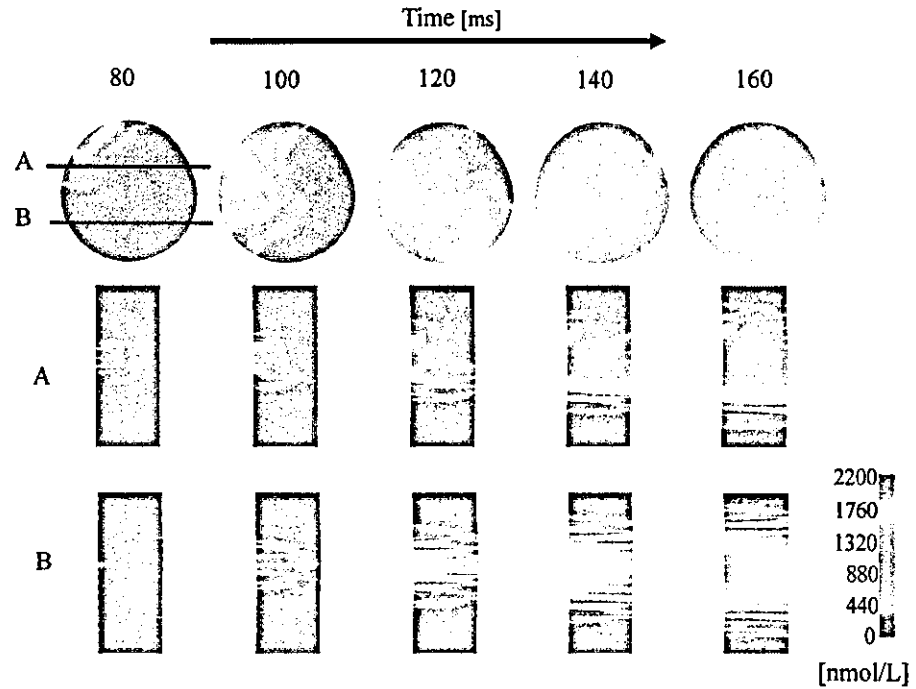
Time [ms]

80   100   120   140   160

Fig. 9. The numbers below the long arrow indicate the elapsed time after the initial Ca^{2+} release. *Top*: short-axis view including the nucleus. A Ca^{2+} wave originating from the proximity of the nucleus spreads around the nucleus to form a spiral wave. *Middle* (*A*): longitudinal section simulating confocal microscopy for a slice including the nucleus (*A* in short-axis view). The formation of a spiral wave is observed around the nucleus. *Bottom* (*B*): longitudinal section for a slice without the nucleus (*B* in short-axis view). The Ca^{2+} wave propagates homogeneously.

2200
1760
1320
880
440
0

[nmol/L]

tations in computer power. It has been shown that spontaneous Ca^{2+} release can cause membrane depolarization that sometimes induces an action potential (6). To analyze this potentially arrhythmogenic event, more comprehensive models that include ion channels and exchangers are needed.

Because of a lack of experimental data, the nucleus was treated as a region lacking a Ca^{2+} release store and a site for Ca^{2+} buffering. However, judging by the complex wave pattern around the nucleus reported in the literature (15, 21), the nucleus may have another role in cytosolic Ca^{2+} regulation. Further experimental evaluation of not only this aspect but also anisotropy in diffusion (12, 31) and Ca^{2+} buffering will surely contribute to the development of a complete model of cardiomyocytes.

Summary. To simulate Ca^{2+} wave propagation in cardiomyocytes, a finite element simulation program incorporating Ca^{2+} diffusion and excitation-contraction coupling mechanisms was developed. The results clearly indicate the 3-D nature of this phenomenon, the modulatory effect of contraction, and the role of the nucleus in the evolution of complex wave patterns.

APPENDIX: FORMULATION OF THE MODEL

1) Ca^{2+} dynamics
At the NSR node:

$$\frac{d[Ca^{2+}]_{total}}{dt} = \nabla \cdot (D_c \nabla[Ca^{2+}]_i) + (I_{leak} - I_{up}) \frac{V_{NSRnode}}{V_{myonode}} :$$

Ca^{2+} balance in the cytoplasm

$$\frac{d[Ca^{2+}]_{NSR}}{dt} = I_{up} - I_{leak} - I_{tr} \cdot \frac{V_{JSRnode}}{V_{NSRnode}} : Ca^{2+} \text{ balance in the NSR}$$

$$I_{up} = \frac{I_{up} \cdot [Ca^{2+}]_i}{([Ca^{2+}]_i + K_{m,up})} : Ca^{2+} \text{ uptake by the NSR}$$

$$I_{leak} = \frac{I_{up}}{[Ca^{2+}]_{NSR}} [Ca^{2+}]_{NSR} : Ca^{2+} \text{ leakage from the NSR}$$

$$I_{tr} = \frac{([Ca^{2+}]_{NSR} - [Ca^{2+}]_{JSR})}{\tau_{tr}} :$$

Translocation of Ca^{2+} from the NSR to the JSR

At the JSR node:

$$\frac{d[Ca^{2+}]_{total}}{dt} = I_{relCICR} \frac{V_{JSRnode}}{V_{myonode}} + \nabla \cdot (D_c \nabla[Ca^{2+}]_i) :$$

Ca^{2+} balance in the cytoplasm

$$[Ca^{2+}]_{JSR,total} = [Ca^{2+}]_{JSR} + [CSQN - Ca^{2+}] : \text{Total } Ca^{2+} \text{ in the JSR}$$

$$[CSQN - Ca^{2+}] = \frac{[CSQN] \cdot [Ca^{2+}]_{JSR}}{([Ca^{2+}]_{JSR} + K_{m,CSQN})} :$$

Calsequestrin (CSQN) Ca^{2+} buffering in the JSR

$$\frac{d[Ca^{2+}]_{JSR,total}}{dt} = I_{tr} - I_{relCICR} : Ca^{2+} \text{ balance in the JSR}$$

$$I_{relCICR} = G_{relCICR} \cdot ([Ca^{2+}]_{JSR} - [Ca^{2+}]_i) :$$

Ca^{2+}-induced Ca^{2+}release (CICR) from the JSR;

$G_{relCICR} = 0$ when $[Ca^{2+}] <$ the threshold level

$$G_{relCICR} = \bar{G}_{relCICR} \cdot \left[1 - exp\left(-\frac{t}{\tau_{on}}\right)\right] \cdot \left[exp\left(-\frac{t}{\tau_{off}}\right)\right]$$

when $[Ca^{2+}] \geq$ the threshold level; $t = 0$ at the onset of CICR

For both the NSR and JSR nodes:

$$[Ca^{2+}]_{total} = [Ca^{2+}]_i + [TnC - Ca^{2+}] + [CaM - Ca^{2+}] :$$

Total Ca^{2+} in the cytoplasm

2) Ca^{2+} buffering in the cytoplasm
CMDN:

$$[CaM - Ca^{2+}] = \frac{[\overline{CaM}] \cdot [Ca^{2+}]_i}{([Ca^{2+}]_i + K_{m,CaM})}$$

(Fast buffering was assumed; see text for details.)

TnC:

$$[TnC - Ca^{2+}] = [TCa] + [TCa*]:$$

Total amount of TnC bound to Ca^{2+}

$$\frac{d[TCa]}{dt} = Q_b - Q_a$$

$$\frac{d[TCa*]}{dt} = Q_a - Q_r - Q_{d2}$$

$$\frac{d[T*]}{dt} = Q_r - Q_d - Q_{d1}$$

$$[T] = [\overline{T}] - [TCa] - [TCa^{2+}] - [T*]$$

$$Q_b = Y_1 \cdot [Ca^{2+}]_i \cdot [T] - Z_1 \cdot [TCa]$$

$$Q_a = Y_2 \cdot [Ca^{2+}]_{eff} - Z_2 \cdot [TCa*]$$

$$[TCa]_{eff} = [TCa] \cdot exp[-R(L - L_a)^2]$$

$$Q_r = Y_3 \cdot [TCa*] - Z_3 \cdot [T*] \cdot [Ca^{2+}]_i$$

$$Q_d = Y_4 \cdot [T*]$$

$$Q_{d1} = Y_d \cdot \left(\frac{dX}{dt}\right)^2 \cdot [T*]$$

$$Q_{d2} = Y_d \cdot \left(\frac{dX}{dt}\right)^2 \cdot [TCa*]$$

At nodes including the nucleus:

$$\frac{d[Ca^{2+}]_{total}}{dt} = -I_{nucleus} \frac{V_{NSRnode}}{V_{myonode}} + \nabla \cdot (D_c \nabla[Ca^{2+}]_i)$$

$$I_{nucleus} = \frac{I_{nucleus} \cdot [Ca^{2+}]_i}{([Ca^{2+}]_i + K_{m,nucleus})} : Ca^{2+} \text{ uptake by the nucleus}$$

3) Mechanical properties of myofibrils

$$F = F_b + F_p$$

$$F_p = K \cdot (L - L_0)^5$$

$$\frac{dX}{dt} = B \cdot (h - h_c)$$

$$F_b = A \cdot ([TCa*] + [T*]) \cdot h$$

$$h = L - X$$

Definitions of variables: $[Ca^{2+}]_i$, free Ca^{2+} concentration in the cytoplasm (mmol/l); $[Ca^{2+}]_{total}$, total cytoplasmic Ca^{2+} concentration (mmol/l); $[CaM - Ca^{2+}]$, CaM-buffered Ca^{2+} concentration (mmol/l); $[TnC - Ca^{2+}]$, TnC-buffered Ca^{2+} concentration (mmol/l); $[Ca^{2+}]_{NSR}$, NSR Ca^{2+} concentration (mmol/l); $[Ca^{2+}]_{JSR}$, JSR Ca^{2+} concentration (mmol/l); $[Ca^{2+}]_{JSR,total}$, total JSR Ca^{2+} concentration including buffered Ca^{2+} (mmol/l); $[CSQN - Ca^{2+}]$, calsequestrin-buffered Ca^{2+} concentration (mmol/l); I_{up}, Ca^{2+} uptake from the cytoplasm to the NSR (mmol/l/ms); I_{leak}, Ca^{2+} leakage from the NSR to the cytoplasm (mmol/l/ms); I_{tr}, translocation current of Ca^{2+} from the NSR to the JSR (mmol/l/ms); $I_{relCICR}$, Ca^{2+} release from the JSR to the cytoplasm due to CICR (mmol/l/ms); $I_{nucleus}$, Ca^{2+} uptake from the cytoplasm to the nucleus (mmol/l/ms);

$[TCa^{2+}]$, thin filament site with TnC bound to Ca^{2+} (mmol/l); $[TCa^{2+}]_{eff}$, effective $[TCa^{2+}]$ (mmol/l); $[TCa*]$, thin filament site with TnC bound to Ca^{2+} and an attached cross bridge (mmol/l); [T], thin filament site with free TnC (mmol/l); [T*], thin filament site with an attached cross bridge and without Ca^{2+} bound to TnC (force generator) (mmol/l); Q_b, net rate of Ca^{2+} binding to T (mmol/l/ms); Q_a, net rate of cross-bridge attachment; Q_r, net rate of Ca^{2+} release from TCa* (mmol/l/ms); Q_d, rate of T* detachment to give Ca^{2+} and T (mmol/l/ms); Q_{d1}, additional rate of T* detachment during filament sliding (mmol/l/ms); Q_{d2}, additional rate of TCa* detachment during filament sliding (mmol/l/ms); F_b, equivalent cross-bridge force normalized with respect to the muscle cross-sectional area (kPa); F_p, elastic force in parallel with F_b normalized with respect to the muscle cross-sectional area (kPa); F, force developed by a muscle unit normalized with respect to the muscle cross-sectional area (kPa); $K_{m,up}$, half-concentration saturation of I_{up}; L, half-sarcomere length (μm); h, cross-bridge elongation (μm); X, length composed of half of the thick filament and the free portion of the thin filament (μm); $VNSR_{node}$ and $VJSR_{node}$, NSR and VSR volume for each FE node, respectively; $V_{myonode}$, cytoplasm volume for each FE node.

REFERENCES

1. **Backx PH, de Tombe PP, Van Deen JHK, Mulder BJM, and ter Keurs HEDJ.** A model of propagating calcium-induced calcium release mediated by calcium diffusion. *J Gen Physiol* 93: 963–977, 1989.
2. **Berlin JR, Cannell MB, and Lederer WJ.** Cellular origins of the transient inward current in cardiac myocytes: role of fluctuations and waves of elevated intracellular calcium. *Circ Res* 65: 115–126, 1989.
3. **Bers DM.** Control of cardiac contraction by SR and sarcolemmal Ca fluxes. *Excitation-Contraction Coupling and Cardiac Contractile Force* (2nd ed.). Dordrecht, The Netherlands: Kluwer Academic, 2001, p. 245–272.
4. **Bers DM.** Sources and sinks of activator calcium. *Excitation-Contraction Coupling and Cardiac Contractile Force* (2nd ed.). Dordrecht, The Netherlands: Kluwer Academic, 2001, p. 39–62.
5. **Bonet J and Burton AJ.** A simple orthotropic, transversely isotropic hyperelastic constitutive equation for large strain computations. *Comput Methods Appl Mech Eng* 162: 151–164, 1998.
6. **Capogrossi MC, Houser SR, Bakinski A, and Lakatta EG.** Synchronous occurrence of spontaneous localized calcium release from the sarcoplasmic reticulum generates action potentials in rat cardiac ventricular myocytes at normal resting membrane potential. *Circ Res* 61: 498–503, 1987.
7. **Capogrossi MC and Lakatta EG.** Frequency modulation and synchronization of spontaneous oscillations in cardiac cells. *Am J Physiol Heart Circ Physiol* 248: H412–H418, 1985.
8. **Cheng H, Lederer MR, Lederer WJ, and Cannell MB.** Calcium sparks and $[Ca^{2+}]_i$ waves in cardiac myocytes. *Am J Physiol Cell Physiol* 270: C148–C159, 1996.
9. **Cheng H, Lederer WJ, and Cannell MB.** Calcium sparks: elementary events underlying excitation-contraction coupling in heart muscle. *Science* 262: 740–744, 1993.
10. **Dupont G, Pontes J, and Goldbeter A.** Modeling spiral Ca^{2+} waves in single cardiac cells: role of the spiral heterogeneity created by the nucleus. *Am J Physiol Cell Physiol* 271: C1390–C1399, 1996.
11. **Dvorkin EN and Bathe KJ.** A continuum mechanics based four-node shell element for general nonlinear analysis. *Eng Comput* 1: 77–88, 1984.
12. **Engel J, Fechner M, Sowerby AJ, Finch AAE, and Stier A.** Anisotropic propagation of Ca^{2+} waves in isolated cardiomyocytes. *Biophys J* 66: 1756–1762, 1994.
13. **Gordon AM, Homsher E, and Regnier M.** Regulation of contraction in striated muscle. *Physiol Rev* 80: 853–924, 2000.

14. Hannon JD, Martyn DA, and Gordon AM. Effects of cycling and rigor crossbridges on the conformation of cardiac troponin C. *Circ Res* 71: 984–991, 1992.

15. Ishida H, Genka C, Hirota Y, Nakazawa H, and Barry WH. Formation of planar and Ca²⁺ waves in isolated cardiac myocytes. *Biophys J* 77: 2114–2122, 1999.

16. Izu LT, Wier WG, and Balke CW. Evolution of cardiac calcium waves from stochastic calcium sparks. *Biophys J* 80: 103–120, 2001.

17. Kaneko T, Tanaka H, Oyamada M, Kawata S, and Takamastu T. Three distinct types of Ca²⁺ waves in Langendorff-perfused rat heart revealed by real-time confocal microscopy. *Circ Res* 86: 1093–1099, 2000.

18. Keizer J and Levine L. Ryanodine receptor adaptation and Ca²⁺-induced Ca²⁺ release-dependent Ca²⁺ oscillations. *Biophys J* 71: 3477–3487, 1996.

19. Keizer J and Smith GD. Spark-to-wave transition: saltatory transmission of calcium waves in cardiac myocytes. *Biophys Chem* 72: 87–100, 1998.

20. Lin DHS and Yin FCP. A multiaxial constitutive law for mammalian left ventricular myocardium in steady-state barium contracture or tetanus. *J Biomech Eng* 120: 504–517, 1998.

21. Lipp P and Niggli E. Microscopic spiral waves reveal positive feedback in subcellular calcium signaling. *Biophys J* 65: 2272–2276, 1993.

22. Luo CH and Rudy Y. A dynamic model of the cardiac ventricular action potential: I. simulations of ionic currents and concentration changes. *Circ Res* 74: 1071–1096, 1994.

23. Malvern LE. *Introduction to the Mechanics of a Continuous Medium.* Englewood Cliffs, NJ: Prentice-Hall, 1969, p. 34–35.

24. Miura M, Boyden PA, and ter Keurs HEDJ. Ca²⁺ waves during triggered propagated contractions in intact trabeculae: determinants of the velocity of propagation. *Circ Res* 84: 1459–1466, 1999.

25. Negroni JA and Lascano EC. A cardiac muscle model relating sarcomere dynamics to calcium kinetics. *J Mol Cell Cardiol* 28: 915–929, 1996.

26. Orchard CH, Eisner DA, and Allen DG. Oscillations of intracellular Ca²⁺ in mammalian cardiac muscle. *Nature* 304: 735–738, 1983.

27. Parker I, Zang WJ, and Wier G. Ca²⁺ sparks involving multiple Ca²⁺ release sites along Z-lines in rat heart cells. *J Physiol* 497: 31–38, 1996.

28. Smith GD, Wagner J, and Keizer J. Validity of rapid buffering approximation near a point source of calcium ions. *Biophys J* 70: 2527–2539, 1996.

29. Sneyd J, Girard S, and Clapham D. Calcium wave propagation by calcium-induced calcium release: an unusual excitable system. *Bull Math Biol* 55: 315–344, 1993.

30. Stuyvers BD, Boyden PA, and ter Keurs HEDJ. Calcium waves: physiological relevance in cardiac function. *Circ Res* 86: 1016–1018, 2000.

31. Subramanian S, Viatchenko-Karpinski S, Lukyanenko V, Györke S, and Wiesner TF. Underlying mechanisms of symmetric calcium wave propagation in rat ventricular myocytes. *Biophys J* 80: 1–11, 2001.

32. Takamastu T and Wier WG. Calcium waves in mammalian heart: quantification of origin, magnitude, and velocity. *FASEB J* 4: 1519–1525, 1990.

33. Wagner J and Keizer J. Effects of rapid buffers on Ca²⁺ diffusion and Ca²⁺ oscillations. *Biophys J* 67: 447–456, 1994.

34. Wier WG, ter Keurs HEDJ, Marban E, Gao WD, and Balke CW. Ca²⁺ "spark" and waves in intact ventricular muscle resolved by confocal imaging. *Circ Res* 81: 462–469, 1997.

35. Yasuda SI, Sugiura S, Kobayakawa N, Fujita H, Yamashita H, Katoh K, Saeki Y, Kaneko H, Suda Y, Nagai R, and Sugi H. A novel method to study contraction characteristics of a single cardiac myocyte using carbon fibers. *Am J Physiol Heart Circ Physiol* 281: H1442–H1446, 2001.

Finite Element Analysis of Ventricular Wall Motion
and Intra-Ventricular Blood Flow
in Heart with Myocardial Infarction*

Hiroshi WATANABE**, Takeshi SUGANO***, Seiryo SUGIURA** and Toshiaki HISADA**

To study the wall motion abnormality and characteristic flow distribution observed in the heart with myocardial infarction, we modified our finite element model of left ventricle and performed simulations at two different phases after the onset of the disease by applying characteristic material property to the infarcted region. The model could not only reproduce the hemodynamic change in myocardial infarction but also give mechanistic insight into the following complicating problems. 1) Stagnation of blood as the cause of clot formation 2) Extra energy wasted for the stretch of infarcted tissue. The effect of compensatory enhancement of the force generation in normal myocardial tissue is also discussed.

Key Words: Biomechanics, Computational Mechanics, Finite Element Method, Fluid-Structure Interaction Analysis, Heart, Electro-Physiology

1. Introduction

Myocardial infarction is a severe form of ischemic heart disease caused by the acute blocking of coronary circulation leaving serious damage to the myocardial tissue down stream to the blocking site. Because it constitutes a major health problem in the industrial countries, active studies are still underway for the cure and prevention of this disease[1]. Although, of course, clarification of underlying biological mechanism is the key to the complete understanding of this disease, some of its aspects need engineering analysis for their solution.

In myocardial infarction, the non- or poorly contracting affected heart muscle is stretched by the wall tension generated by the contraction of normal muscle. Stretching the muscle not only causes the secondary damage to the infarcted tissue but also demands extra work to the normal tissue thereby leading to the deterioration of the whole ventricle (cardiac remodeling). In addition to the mechanical disorder, stretching of the heart tissue could form a substrate for fatal arrhythmia through the excitation abnormality induced by the mechao-electrical feed-

back mechanims[2]. Both processes are closely linked to the temporal and spatial distribution of stress and strain in the ventricular wall accurate assessment of which can be achieved only by solid mechanics. In this respect, Janz et al.[3], Bogen et al.[4], Guccione et al.[5], and Moustakidis et al.[6] performed finite element method based analyses of ventricular wall with myocardial infarction. Another serious complication of myocardial infarction is the formation of ventricular thrombus, which sometimes detaches and produces systemic arterial embolization. Because the clinical studies have identified close correlation between the thrombus formation and wall motion abnormality[7] and/or flow characteristics in the ventricle[8], engineering analysis could make significant contribution also to the study of this problem.

We have already developed a finite element model of the left ventricle based on the molecular mechanisms of cardiac excitation-contraction[9]−[11]. Because, in these analyses, both structure (ventricular wall) and fluid (blood) were simulated by fluid-structure interaction analysis[11], we could examine the relation between the structure and function of cardiac tissue and hemodynamic parameters in detail. In this study, based on this model, we simulated the heart with myocardial infarction by adopting different material property locally to the affected area of the ventricle. We could successfully reproduce both wall motion abnormality and characteristic flow distribution in the ventricle reported in experimental studies and

clinical observations. Detailed flow distribution and energetic consideration derived from this model analysis will also be discussed.

2. Methods

2.1 Model framework

Details of the formulations have been described in our previous reports[9]-[11]. Here, we briefly present the framework of the comprehensive simulation program based on finite element method. This program is composed of the following four models:

1) Excitation and propagation model: Upon stimulations, myocardial cells are excited and contract to develop force. In this program, the FitzHugh-Nagumo (FHN) model[12],[13], a well-known simple model of membrane action potential, is coupled with the monodomain propagation model[12]-[14].

2) Excitation – contraction (E–C) coupling: After excitation (membrane depolarization), a series of subcellular events lead to a transient increase in intracellular calcium concentration $[Ca^{2+}]$, which in turn controls the interaction of contractile proteins named actin and myosin (cross-bridge kinetics) to develop a force. To describe the dynamic relationship between $[Ca^{2+}]$ and cross-bridge kinetics, a four-state model proposed by Peterson et al.[15] was employed. To connect the membrane depolarization (FHN model) and the four-state model for E–C coupling, a FHN model was used to give a trigger (timing) for the phasic change in Ca^{2+} ion concentration (Ca^{2+}-transient).

3) Material property of cardiac muscles: To characterize the properties of cardiac muscles, we adopted the Lin-Yin model[16] for the constitutive equation which is based on hyperelastic material theory. In this model, the strain energy potential (W) is divided into two components, i.e., passive (W_{pass}), and active (W_{act}) ones. As the E–C coupling model provides active force (F) of the muscle depending on the calculated population of the attached cross-bridges, we can consider the coefficients for the active components in Lin-Yin model to be a function of F, whereas those for the passive components to be constant.

4) Finite element model: The ventricle and the blood are modeled by the fluid-structure interaction (FSI) finite element method which has been developed by us[11],[17]. For the analysis of blood flow, the ALE form of the Navier-Stokes equations are discretized by the stabilized Galerkin (SUPG)[18] method. For the analysis of ventricle, the total Lagrangian formulation is discretized by a standard finite element method, and a nonlinear system of equations is obtained. These equations are strongly coupled so that the full interaction conditions between the fluid and structure are introduced. In addition to the FSI program, our simulator has a function to deal with the ventricle motion only by the structural analysis. In this analysis, the effects of the blood flow are represented only by

the pressure. In other words, the inertial and the viscous terms are neglected in the momentum equation of blood. Also, the inertial effect of the ventricle is neglected. Thus, the FSI program is reduced to a static structural finite element code that models only the cardiac muscles. This analysis will be termed "structure only analysis" hereafter. For precise formulation, see previous study[9].

2.2 FE model of normal LV and its loading conditions

Although it is an essential requirement for FE analysis to determine the mesh of an object based on the initial shape in an undeformed state under stress-free conditions, it is difficult to know this for a living human LV. In the previous study[9]-[11] as well as in this study, we estimated the initial shape of LV from MR images of adult human LV at end-diastole by applying an appropriate negative pressure to it so that the volume becomes 60×10^3 mm^3. This process was done only to make an initial finite element mesh under stress-free state. Then we applied physiological ventricular pressure at end-diastole (1 500 Pa) to obtain the fiber strain at the beginning of contraction. In this study, ventricular wall was divided into six layers. The fiber orientations of the model were -90, -60, -30, 0, 30 and 60 degrees respectively. We used Q1-P0 mixed hexahedral elements (eight nodes for the bilinear velocity or displacement interpolation/constant pressure field) for both the fluid and the structure. The number of solid elements was 9 792, that of fluid elements 18 976, and the total DOF was about 120 000. Numerical convergence of this model was confirmed in the previous study[11]. In the electro-physiological analysis, the same structural mesh was used as an electro-physiological unit. In other words, FHN cell unit is embedded in each finite element, and is electrically connected with the cells surrounding it (see Fig. 1). We assumed isotropic conduction of excitation.

To simulate the systemic arterial tree, the windkessel model[19] was connected to the aortic valve (see Fig. 1). An electric analog model of LA and pulmonary circulation proposed by Alexander et al.[11],[20] was modified and connected to the mitral valve to simulate the preload of LV. In a similar way to the LV, the LA was characterized by the time-varying elastance[20] defined as $E_{LA} = P_{LA}/(q_{LA} - q_0)$, where P_{LA} and q_{LA} are instantaneous pressure and volume of LA, respectively, and q_0 is the volume axis intercept. P_V is the pulmonary source pressure, R_V is the source resistance, C_P is the pulmonary venous capacitance, R_P is the pulmonary resistance, L_P is the pulmonary inertance, R_{AV} is the atrioventricular resistance, L_{AV} is the atrioventricular inertance, F_{RL} is the pulmonary venous flow, F_{Mi} is the blood flow through the mitral valve, q_P is the volume of the pulmonary venous, and P_{LV} is the pressure boundary condition for the FSI model (Fig. 1). The following values are assumed for these parameters: $P_V = 1\,600$ Pa, $R_V = 0.333$ MPa sec/m^3, $C_P = 0.052\,5$ μm^3/Pa,
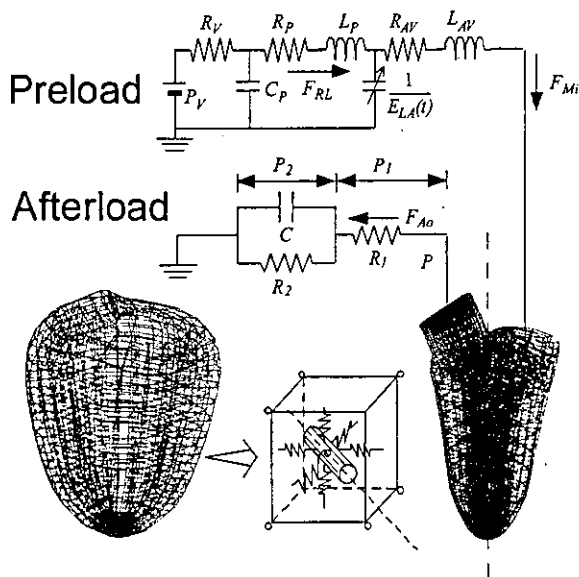
Fig. 1   FE mesh and boundary condition

R_P = 12.0 MPa sec/m³, L_P = 0.133 MPa sec²/m³, R_{AV} = 3.47 MPa sec/m³, L_{AV} = 0.267 MPa sec²/m³. In this analysis, the time course of E_{LA} was defined as follows; 1) in the resting state LAP was a linear function of LAV, i.e., $E_{LA}(t)$ was constant ($E_{LA}(t)$ = 13.3 MPa/m³), 2) the contraction of LA started 0.15 seconds prior to the onset of LV contraction and lasted for 0.2 seconds with a time course represented by a sinusoid whose amplitude is 26.7 MPa/m³.

The coefficients of Lin-Yin constitutive equation (see Eqs. (3) and (4) in section 3) for the cardiac muscles were assumed as follows[9]-[11]: c_1 = 82.4 Pa, c_2 = 7.304, c_3 = 1.856, c_4 = 0.064, c_5^{max} = 0.0, c_6^{max} = -6.39 kPa, c_7^{max} = 18.0 kPa, c_8^{max} = 17.4 kPa, c_9^{max} = 7.61 kPa, c_{10}^{max} = 19.4 kPa. The density of cardiac muscle was assumed to be ρ = 1.37×10³ kg/m³, the density of blood ρ = 1.06×10³ kg/m³, and the viscosity of blood μ = 4.71×10⁻³ Pa sec.

2.3   Simulation

The following boundary and initial conditions were set for each phase of cardiac cycle: During isovolumic contraction (phase 1), both the mitral and aortic valves were closed so that the flow velocity was zero at those two boundaries. The initial value of the volume of LV (LVV) was about 120×10³ mm³ under fully relaxed conditions. Then, the muscles were activated by the excitation-contraction mechanism (represented by the FHN model and the four-state model) to increase the pressure of LV (LVP). When the LVP exceeded the aortic pressure calculated by the windkessel model, the aortic valve opened. During ejection (phase 2), with the mitral valve closed, the pressure boundary condition given by the windkessel model was applied to the open aortic valve area. The FSI FE model and the windkessel model were iteratively calculated to determine the equilibrium state. In the first half of the ejection, pressure gradient between the left ventricle

and aorta accelerates the blood and, due to the inertia, the blood keeps flowing out of the ventricle even if the aortic pressure exceeds the ventricular pressure in the second half of ejection. However, reversed pressure gradient decelerates the blood and finally causes the backward flow. When backward flow occurred in the aorta, the aortic valve closed to finish phase 2. From this point, the windkessel was disconnected from the LV and its state was calculated under the condition that F_{Ao} = 0 until the next cardiac cycle. During isovolumic relaxation (phase 3), the relaxation of cardiac muscles proceeded while both the aortic and mitral valves closed. When the LVP fell below the left atrial pressure (LAP) calculated by the Alexander model, the mitral valve opened and ventricular filling (phase 4) began. Heart rate was set at 60 beats per minute (one cardiac cycle = 1.0 sec). In the case of structure only analysis, the flows though aortic and mitral valves were obtained from the volume change rate of LV. Based on these assumptions, we calculated four cardiac cycles in the case of FSI analysis, and five cardiac cycles in case the of structure only analysis.

We have tested the performance of this model by comparing some of its results with the clinical data reported in literatures. These are: intra-ventricular and aortic pressures and the ventricular pressure-volume relation during the cardiac cycle[9], rotation and vertical displacement of the ventricle[10], diastolic flow propagation velocity obtained from the flow mapping[11]. All of these comparisons demonstrated good agreement thus supporting the validity of this model. Based on the verification made on normal heart, we attempted to develop a diseased heart model in this study.

3.   FE Model of Ventricle with Myocardial Infarction

When a poorly collateralized anterior descending coronary artery is totally occluded, severely damaged ventricular wall composed of fibrous tissue, necrotic tissue, and slightly remaining viable cardiac muscle is stretched and becomes thinner and bulges in each contraction[1]. To simulate this condition termed as ventricular aneurysm, we modeled a case in which anterior descending coronary artery was occluded in its middle portion. According to the anatomy of coronary arteries, affected region of the ventricular wall from such an insult would extend from the apex to the middle of LV longitudinally and from the middle of the ventricular septum to diagonal branch circumferentially[21]. The shape and the wall thickness of the infarcted region were adopted from the MR image data reported in the literature (5). In the present model of myocardial infarction, infarcted region amounted to 40% of the total LV wall. Because we assumed 10% of the border zone, having the material property between normal and infarcted tissue, surrounding the infarcted region, 50% of the ventricular wall remained normal (Fig. 2). Wall thick-

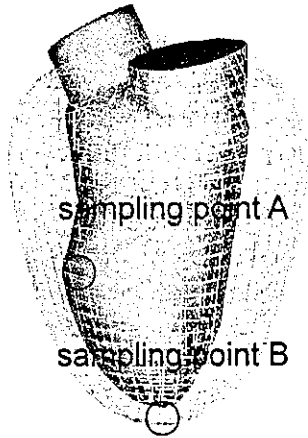Fig. 2 Distribution of normal, infarcted, and border zone regions

Fig. 3 FE model of LV with myocardial infarction

ness of the infarcted region was set at 50% of the normal region (Fig. 3).

In infarcted region of the ventricular wall, both passive and active properties of the tissue change depending on the time after the onset. In the animal model of myocardial infarction, Rabinowitz et al.[22] reported that the passive stiffness of the cardiac muscle decreases in the early phase (1-hour) of infarction, but it progressively increases over a period of days to weeks. Based on these experimental results, Bogen et al.[4] proposed the following uniaxial constitutive equation:

$$\sigma = \mu_p(\lambda^{k_p} - \lambda^{-k_p/2}) \qquad (1)$$

Parameters for normal, acute and subacute infarction are $\mu_p = 2$, $k_p = 16$, $\mu_p = 7.9$, $k_p = 13$, and $\mu_p = 0.8$, $k_p = 31$, respectively. To reproduce these stress-strain relations by hyperelasticity based constitutive law, we modified the Lin-Yin model by adding the extra potential term proposed by Humphrey et al.[23]

$$W_{total} = W_{pass} + W_{act} + mW_{pass\_humph}, \qquad (2)$$

$$W_{pass} = c_1(e^Q - 1),$$
$$Q = c_2(I_1 - 3)^2 + c_3(I_1 - 3)(I_4 - 1) + c_4(I_4 - 1)^2, \qquad (3)$$

$$W_{act} = c_5 + c_6(I_1 - 3)(I_4 - 1) + c_7(I_1 - 3)^2$$
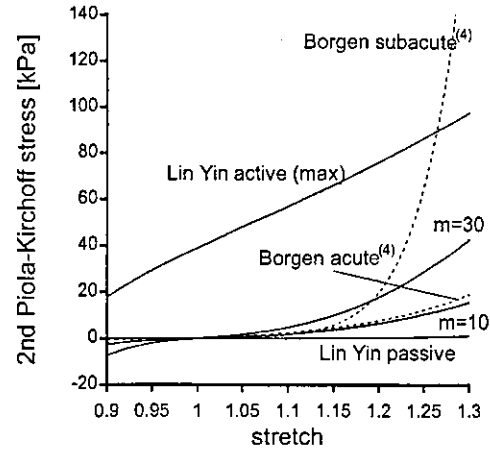$$+ c_8(I_4 - 1)^2 + c_9(I_1 - 3) + c_{10}(I_4 - 1), \qquad (4)$$

Fig. 4 Stress-stretch relationship

$$c_5 = Fc_5^{max}, \quad c_6 = Fc_6^{max}, \quad c_7 = Fc_7^{max},$$
$$c_8 = Fc_8^{max}, \quad c_9 = F^2 c_9^{max}, \quad c_{10} = F^2 c_{10}^{max}, \qquad (5)$$

$$W_{pass\_humph} = c_{1h}(I_4^{\frac{1}{2}} - 1)^2 + c_{2h}(I_4^{\frac{1}{2}} - 1)^3 + c_{3h}(I_1 - 3)$$
$$+ c_{4h}(I_1 - 3)(I_4^{\frac{1}{2}} - 1) + c_{5h}(I_1 - 3)^2, \qquad (6)$$

where the parameters of Humphrey-Yin model are $c_{1h} = 1.97$ kPa, $c_{2h} = 6.21$ kPa, $c_{3h} = 0.164$ kPa, $c_{4h} = -2.70$ kPa, $c_{5h} = 2.35$ kPa. Since the stretch in fiber direction takes the value between 0.85 and 1.25 in normal case, in Eq. (2) the value of 'm' was selected 10.0 and 30.0 in the cases of acute and subacute infarction, respectively, to fit the stress-stretch curves in this range. In Fig. 4, the reproduced uniaxial stress-strain relationships in the fiber direction are shown. For the border zone, same material property as that of normal region was given.

As the cardiac contractility is depressed in the infarcted region, the activations of (F) infarcted and border zone regions were set at 30 and 70% relative to the normal region respectively.

It is well known that the preload and afterload are varied by the compensation. However, because the objective of this paper is to elucidate the difference of the mechanical behavior of heart in normal and diseased case exclusively, the parameters of preload and afterload models are set at the same values as the normal case. Based on this model, the effect of the compensation of preload and afterload should be incorporated in the future modeling.

4. Results

4.1 Fluid-structure interaction analysis of acute infarction model

Figure 5 compares the pressure-volume loops of LV obtained by FSI (solid line) and structure only (broken line) analyses. Two loops are in good agreement indicating that the structure only analysis gives fairly good approximation for the study of global (ventricular level) hemodynamics. Time-lapse images of LV contraction and resultant blood flow are shown in Fig. 6 together with the

color-coded presentation of the activation level (normalized F) of the myocardial tissue. While the normal region of the wall becomes thick as it is activated (indicated in red), the infarcted region remains inactivated (indicated in blue) or rather being stretched to become thinner and bulge (aneurysm formation). In the ventricular aneurysm, the flow velocity is low throughout the cardiac cycle. We quantitatively compared the flow velocities computed in infracted and normal cases. Namely, time-averages of flow velocity at the node nearest to the center of aneurysm are taken during systole and diastole, respectively, and they are compared with those of the corresponding node in normal model. During systole they were (10.0 cm/sec in infracted case, 15.6 cm/sec in normal case), and during diastole (5.16 cm/sec, 9.10 cm/sec). These results suggest the causal relation between aneurysm formation and ventricular thrombus via blood stagnation. Indeed, in a

study using Doppler echocardiography, Maze et al.[24] examined the flow characteristics in the patients with dilated cardiomyopathy with and without apical thrombus to find that the flow velocities during both diastole (11.7 ± 15.3, 28.3±10.5 cm/sec) and systole (7.1±8.1, 15.3±7.0 cm/sec) were significantly lower for the thrombus group. To further examine the flow abnormality in myocardial infarction and gain mechanistic insight into it, we compared the intra-ventricular flow and pressure distribution between infarction and normal cases in Fig. 7. During systole
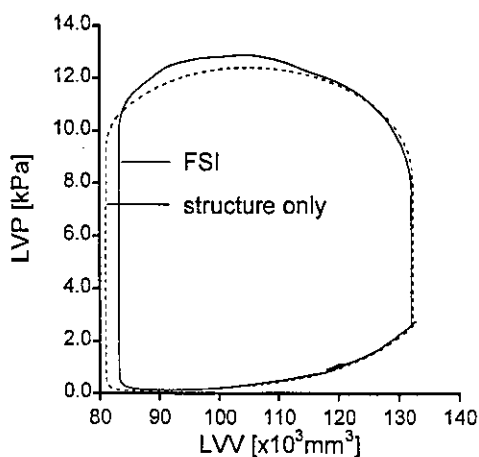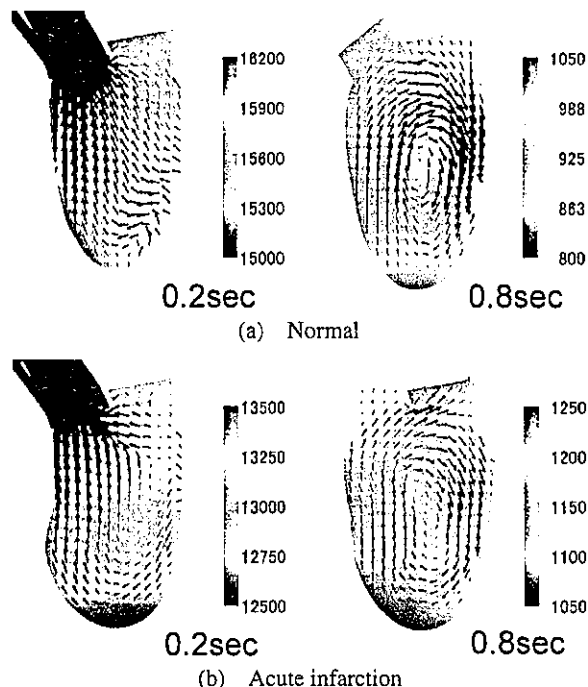

Fig. 5   Pressure-volume loop

Fig. 7   Intra-ventricular flow pattern and pressure distribution
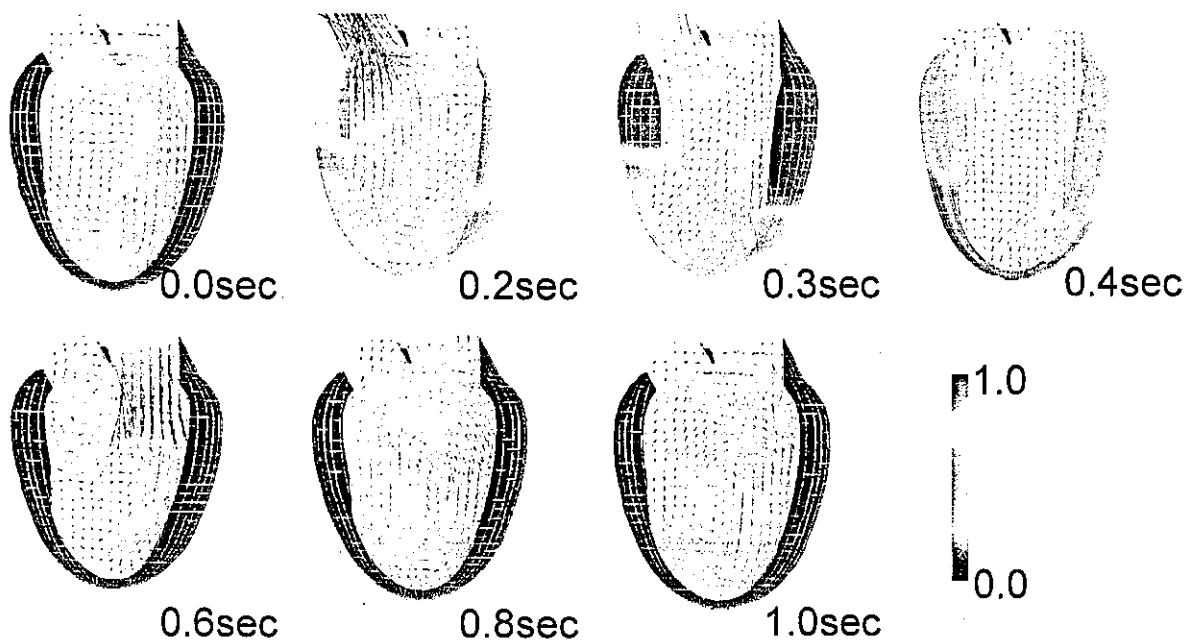

Fig. 6   Intra-ventricular flow pattern

(0.2 sec), whole ventricle was filled with ejection flow directing the aortic valve in normal case. On the other hand, in infarction, ejection flow existed only in the upper half, rather, even the flow directing toward the apex was observed. In normal case, monotonous pressure gradient was formed from the apex to aortic valve, whereas, in infarction, pressure was highest in the upper portion of the ventricle where normal myocardial tissue generated contraction force. During diastole (0.8 sec) large vortices were observed in both cases, but, in acute infarction, the vortex is distorted and its center was shifted toward the apex. These findings are in good agreement with the clinical observation by echocardiograph by Van Dantzig et al.[8] The above observations are further exemplified in Fig. 8, where flows in lateral and longitudinal cross sections in acute and normal cases are compared.

4.2 Energetic efficiency of cardiac muscle

As shown in the previous section (Fig. 5), the FSI analysis and the structure only analysis showed the same trend in terms of global hemodynamic parameters. We therefore use the structure only analysis in the following investigation to save the CPU time. In infarction models, it
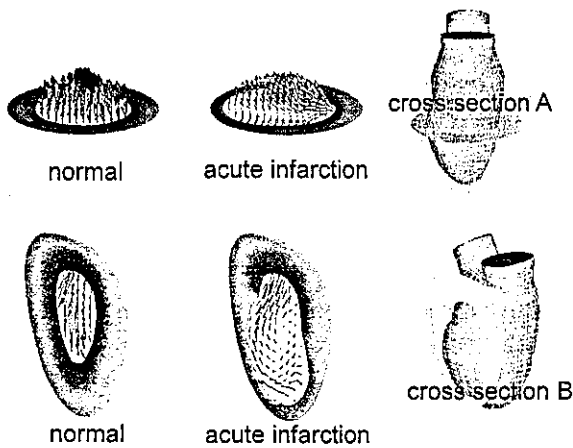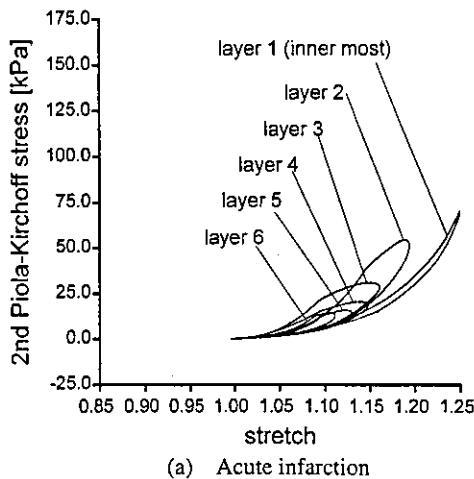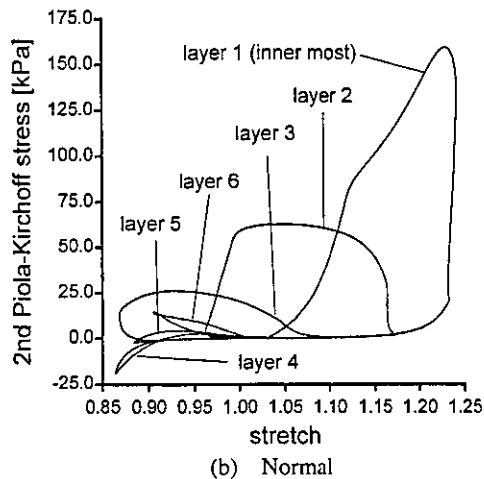
was found that the contraction of the normal cardiac muscle stretches the myocardial tissue in the infarcted region during systole. Figure 9 (a) shows the stress-strain loop of the myocardial fiber in infarcted region (sampling point B in acute model, Fig. 3), and Fig. 9 (b) shows the stress-strain loop at same sampling point of normal model. It shows that the area of stress-strain loop, i.e., work, is almost zero or takes negative value. Negative work means that this specific fiber absorbs work done by active contraction of the normal muscle and reduces the net work output of the whole ventricle. We, therefore, calculated the energetic efficiency defined by Eqs. (7)–(9), i.e., the ratio of the network of ventricular wall that is done for fluid (it was confirmed numerically this work is exactly the same as the area of P-V loop in our FE analysis) to the total work of ventricular wall that is done for fluid and absorbed within ventricular wall. It was 82.1% for normal case, 68.3% for acute infarction and 71.2% for subacute infarction. Such reduction in energy efficiency, at least in part, could be a cause of the deterioration of the whole ventricle in the long run.

Fig. 8   Intra-ventricular flow pattern

$$efficiency = \frac{-\int_V \oint dWdV}{-\int_V \oint 1(-dW)dWdV}, \qquad (7)$$

$$dW = S : dE, \qquad (8)$$

$$1(x) = \begin{cases} 0 & x < 0 \\ 1 & x \geq 0 \end{cases}. \qquad (9)$$

where, S is the second Piola-Kirchoff stress, E the Green-Lagrange strain, and $1(x)$ the unit step function.

4.3 Compensatory mechanisms in myocardial infarction

Myocardial infarction causes significant impairment of cardiac pump function and sometimes threatens patient survival. To maintain the homeostasis under such conditions, human body resorts to various compensatory mech-

(a)   Acute infarction

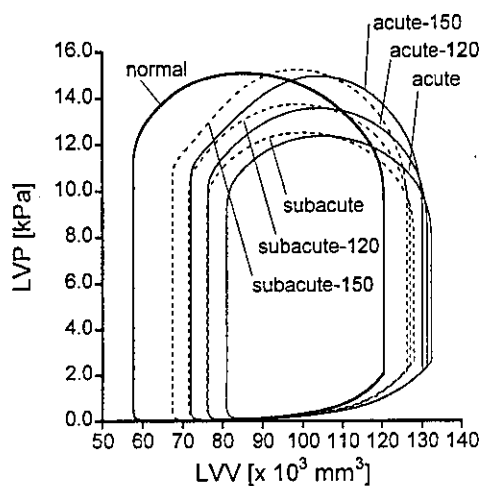(b)   Normal

Fig. 9   Stress-stretch loop

Fig. 10 Pressure-Volume loop

anisms including the enhancement of contractility of the remaining normal myocardial tissue through neural and humoral stimulation. We simulated this mechanism to study its effect in myocardial infarction.

Figure 10 shows the series of P–V loops produced by the normal, acute and subacute infarction model. It may seem strange that the end diastolic volumes of acute and subacute infarction were larger than that of normal case despite their stiffer passive material properties (Fig. 4). This was caused by the thinning of wall in infarcted cases, which made the ventricle as a whole more compliant. Ejection fraction became smaller due to the loss of contraction force and stretch of cardiac muscle in infarcted region absorbing the work done by the normal myocardium as shown above. As a result, the net work output calculated as the area circumscribed by each loop dropped dramatically thus necessitating the compensatory response. To simulate the compensatory response, we increased the contraction force of the normal region by 120 and 150% and showed the resultant P–V loops also in Fig. 10. Hereafter these models are referred as acute-120, acute-150, subactute-120, and subacute-150. It is shown that the ejection fractions recovered by compensation as; (acute 38.8%, acute-120 41.9%, acute-150 44.7%), (subacute 40.5%, subacute-120 43.7%, subacute-150 46.6%), where the ejection fraction of normal heart was 52.2%. However, if we calculate again the energetic efficiency for each case, we find that the efficiency decreases as the compensation progresses as; (acute 68.3%, acute-120 67.7%, acute-150 64.7%), (subacute 71.2%, subacute-120 70.0%, subacute-150 66.5%). As stated in section 4.2, the energetic efficiency of normal heart was 82.1%. It is clear that compensatory enhancement of the function of the remaining viable myocardium works effectively to recover work output of the heart to maintain life of the affected individual, but we must be aware that these improvements were achieved at the expense of energetic inefficiency.

5. Conclusions

To study the abnormal wall motion and intraventricular flow in LV with myocardial infarction, a simulation program was developed by modifying our FE model of LV. By adopting different material properties for passive and active myocardium and giving thinner wall thickness to the infarcted region of the ventricle as reported in the literature, we could reproduce characteristic wall motion, aneurysm formation, and stagnated flow that are clinically observed at acute and subacute phases of infarction. Furthermore, the relation between compensatory enhancement of the remaining viable myocardial tissue and energetic efficiency was discussed.

References

(1) Braunwald, E., Part IV Hypertensive and Atherosclerotic Cardiovascular Disease, Heart Diseases 6th Edition, Edited by Braunwald, E., Zipes, D.P. and Libby, P., (2001), pp.941–1231, W.B. Saunders, Philadelphia.

(2) Frantz, M.R., Cima, R., Wang, D., Profitt, D. and Kurz, R., Electrophysiological Effects of Myocardial Stretch and Mechanical Determinants of Stretch-Activated Arrhythmias, Circulation, Vol.86 (1992), pp.968–978.

(3) Janz, R.F. and Waldron, R.J., Predicted Effect of Chronic Apical Aneurysms on the Passive Stiffness of the Human Left Ventricle, Circ. Res., Vol.42 (1978), pp.255–263.

(4) Bogen, D.K., Rabinowitz, S.A., Needleman, A., Mcmahon, T.A. and Abelmann, W.H., An Analysis of the Mechanical Disadvantage of Myocardial Infarction in the Canine Left Ventricle, Circulation Research, Vol.47 (1980), pp.728–741.

(5) Guccione, J.M., Moonly, S.M., Moustakidis, P., Costa, K.D., Moulton, M.J., Ratcliffe, M.B. and Pasque, M.K., Mechanism Underlying Mechanical Dysfunction in the Border Zone of Left Ventricular Aneurysm: A Finite Element Model Study, Ann. Thorac. Surg., Vol.71 (2001), pp.654–662.

(6) Moustakidis, P., Maniar, H.S., Cupps, B.P., Absi, T., Zheng, J., Guccione, J.M., Sundt, T.M. and Pasque, M.K., Altered Left Ventricular Geometry Changes the Border Zone Temporal Distribution of Stress in an Experimental Model of Left Ventricular Aneurysm: A Finite Element Model Study, Circulation, Vol.106, Supplement 1 (2002), p.168.

(7) Ascione, L., Antonini-Canterin, F., Macor, F., Cervesato, E., Chiarella, F., Giannuzzi, P., Temporelli, P.L., Gentile, F., Lucci, D., Maggioni, A.P., Tavazzi, L., Badano, L., Stoian, I., Piazza, R., Bosimini, E., Pavan, D. and Nicolosi, G.L., Relation between Early Mitral Regurgitation and Left Ventricular Thrombus Formation after Acute Myocardial Infarction: Results of the GISSI-3 Echo Substudy, Heart, Vol.88 (2002), pp.131–136.

(8) Van Dantzig, J.M., Delemarre, B.J., Bot, H., Koster, R.W. and Visser, C.A., Doppler Left Ventricular Flow Pattern versus Conventional Predictors of Left Ventricular Thrombus after Acute Myocardial Infarction,